UNIVERSITÄT AUGSBURG
Universitätsbibliothek

OPEN ACCESS
OPUS AUGSBURG

Two-dimensional reconstruction of filament temperatures and densities with the thermal helium beam at ASDEX Upgrade

D. Wendler, Gregor Birkenmeier, M. Griener, R. Dux, R. Fischer, D. Stieglitz, E. Wolfrum, U. Stroth

Angaben zur Veröffentlichung / Publication details:

Wendler, D., Gregor Birkenmeier, M. Griener, R. Dux, R. Fischer, D. Stieglitz, E. Wolfrum, and U. Stroth. 2023. "Two-dimensional reconstruction of filament temperatures and densities with the thermal helium beam at ASDEX Upgrade." *Physics of Plasmas* 30 (9): 092509. https://doi.org/10.1063/5.0164057.

Nutzungsbedingungen / Terms of use:

CC BY 4.0

Dieses Dokument wird unter folgenden Bedingungen zur Verfügung gestellt: / This document is made available under these conditions:
CC-BY 4.0: Creative Commons: Namensnennung
Weitere Informationen finden Sie unter: / For more information see:
https://creativecommons.org/licenses/by/4.0/deed.de

Physics of Plasmas

RESEARCH ARTICLE | SEPTEMBER 18 2023

Two-dimensional reconstruction of filament temperatures and densities with the thermal helium beam at ASDEX Upgrade

D. Wendler ; G. Birkenmeier ; M. Griener ; R. Dux ; R. Fischer; D. Stieglitz ; E. Wolfrum ; U. Stroth ; ASDEX Upgrade Team

Check for updates

Phys. Plasmas 30, 092509 (2023)
https://doi.org/10.1063/5.0164057

View Online
Export Citation

Articles You May Be Interested In

Impact of divertor neutral pressure on confinement degradation of advanced tokamak scenarios at ASDEX Upgrade

Phys. Plasmas (February 2024)

Comparative study of magnetic reconnection rates in ASDEX Upgrade and EAST tokamaks

Phys. Plasmas (February 2025)

Thermal helium beam diagnostic for 2D profile measurements in the divertor of ASDEX Upgrade

Rev. Sci. Instrum. (November 2024)

04 November 2026 08:21:20

AIP Publishing

Physics of Plasmas

Special Topics Open for Submissions

Learn More

AIP Publishing

Two-dimensional reconstruction of filament temperatures and densities with the thermal helium beam at ASDEX Upgrade

Cite as: Phys. Plasmas **30**, 092509 (2023); doi: 10.1063/5.0164057
Submitted: 20 June 2023 · Accepted: 25 August 2023 ·
Published Online: 18 September 2023

View Online Export Citation CrossMark

D. Wendler,[1,2,a] G. Birkenmeier,[1,2] M. Griener,[1] R. Dux,[1] R. Fischer,[1] D. Stieglitz,[1] E. Wolfrum,[1] U. Stroth,[1,2] and ASDEX Upgrade Team[b]

AFFILIATIONS

[1]Max-Planck-Institut für Plasmaphysik, Boltzmannstr. 2, 85748 Garching, Germany
[2]Physics Department, TUM School of Natural Sciences, Technical University of Munich, 85748 Garching, Germany

[a]**Author to whom correspondence should be addressed:** daniel.wendler@ipp.mpg.de
[b]See the author list in Ref. 57.

ABSTRACT

In the scrape-off layer (SOL) of fusion plasmas, radial particle and energy transport is mainly carried by plasma filaments. The plasma parameters of such filaments can be measured by the thermal helium beam diagnostic (THB). By means of an extended collisional radiative model (CRM) used for the evaluation of the diagnostic data, the light intensity response of neutral helium transitions from filaments is studied, which depends on the parameters of the filament and the background. The electron density of the filament is found to be the dominant parameter impacting the line intensities. By applying a numerical reconstruction algorithm based on the CRM, electron temperatures and densities as well as the sizes of experimentally measured filaments are obtained. This method allows for the first time measurements of the temporal decay rates of filament density and temperature in the co-moving frame of the filament and its radial propagation velocity.

© 2023 Author(s). All article content, except where otherwise noted, is licensed under a Creative Commons Attribution (CC BY) license (http://creativecommons.org/licenses/by/4.0/). https://doi.org/10.1063/5.0164057

04 November 2026 08:21:20

I. INTRODUCTION

Filaments are field aligned structures in the scrape-off layer (SOL) appearing in all tokamak regimes.[1–4] Due to the positive density perturbation associated with filaments, they get electrically polarized, which leads to a radial motion outward.[5–7] By this, filaments contribute significantly to the perpendicular convective transport in the SOL.[8,9] They can be observed by various diagnostics, like gas-puff imaging (GPI),[10–14] Langmuir probes,[15–17] and the lithium beam diagnostic.[18,19] As these diagnostics rely on different measurement principles, they can access different filament properties. So far, Langmuir probes are the most frequently used diagnostic capable of simultaneously measuring filament temperature and density,[20,21] having the disadvantage that their local measurement has reduced 2D capabilities to trace the filament motion and they potentially perturb the plasma.[22,23]

A relatively new diagnostic for evaluating filaments is the thermal helium beam diagnostic (THB).[2] It enables the measurement of the line emission perturbation caused by the filament, radially tracing them in the SOL analogous to GPI. In contrast to using a single atomic transition or a sum of multiple transitions, as GPI does, the THB measures four helium transitions, enabling the reconstruction of edge electron temperature and density profiles.[24,25] At RFX-mod, the THB was used to determine filament temperatures and densities at a fixed position.[26]

In this work, an existing collisional radiative model (CRM)[27] is extended to calculate non-monotonic two dimensional temperature and density profiles and to reconstruct filament amplitudes as well as the size of filaments on short time scales. The paper is organized as follows: In Sec. II, the hardware setup and the collisional radiative model are briefly explained. In Sec. III, the modifications to the CRM are described, and the model is used to study the diagnostic response to artificial filaments in Sec. IV. In Sec. V, the model is applied to a single experimental time point, while an entire time trace is analyzed in Sec. VI.

II. EXPERIMENTAL SETUP AND COLLISIONAL RADIATIVE MODELS

A detailed description of the experimental setup can be found in Ref. 28. The THB diagnostic at ASDEX Upgrade (AUG) is located below the outer midplane, consisting of a piezo valve and an optical

© Author(s) 2023

head, displayed in Fig. 1. The helium injected by the valve leads to line emission due to its interaction with the plasma, which is collected by the optical head, consisting of two lenses. Through the optical head, a 5×5 grid of lines of sight, with additional radial lines of sight, are measured. The angle between the magnetic field (equilibrium from #40425, t = 4.78 s) and the LOS is between 6° and 9°, as shown in Fig. 18.

The collected emission is then guided to a polychromator system, which measures the 587, 667, 706, and 728 nm lines of the helium spectrum. Each spectral line radiance, also referred to as intensity, is then measured by a photomultiplier, sampled with 900 kHz. The helium puff is modulated with 10 Hz, allowing to determine the passive background of the He I lines.

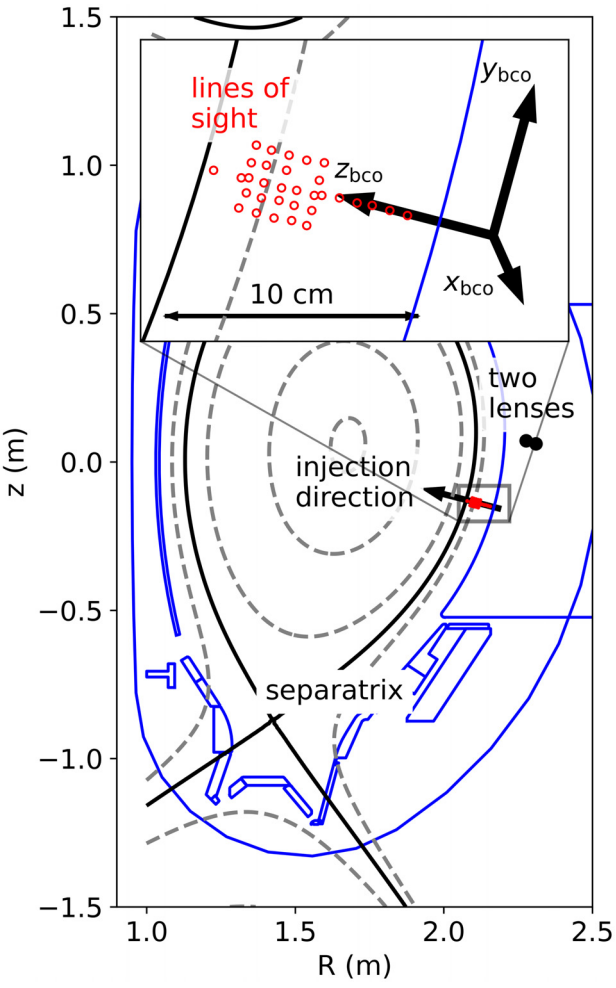


FIG. 1. Cross section of ASDEX Upgrade including the helium beam geometry. The lenses of the optical head are located at a toroidal angle of 17° with respect to the valve and the indicated measurement positions. The beam coordinate system is displayed in the enlarged window. z_{bco} points in the direction of the helium injection, x_{bco} goes along the central line of sight, and y_{bco} is binormal to the other two vectors. The magnetic equilibrium with its poloidal flux surfaces is shown in gray, the separatrix in black, for #40425 and $t = 4.78$ s.

For the evaluation of the measured line intensities, two collisional radiative models are used at AUG to calculate the electron temperature T_e and electron density n_e.

The first model, called the "static model," is based on the assumption of a collisional radiative equilibrium (CRE).[29] This allows to evaluate line ratios, formed from different spectral lines, upon each experimental measurement point enabling the determination of the temperature and density values at the emission position by comparing them to the photo emission coefficients (PECs). The corresponding relation of temperature and density to certain line ratios is shown in Appendix, Fig. 17. By using line ratios, the neutral helium density is irrelevant for the evaluation. The static model is valid over a wide radial range in the edge. However, at the outermost radial region directly after the injection, the model leads to an artificial temperature rise, caused by the fact that the assumption of a CRE does no longer hold. To correct this effect, a new model, called "dynamic model," was developed.[27]

The dynamic model is based on a dynamic approach for the state populations, discarding the assumption of the previously mentioned collisional radiative equilibrium.[27] The model calculates for given temperature and density profiles the radiance of the helium cloud. The cloud is given by a Gaussian neutral density distribution,[30] which is reduced by the time-dependent ionization of the helium, calculated within the forward model. By integrating the radiance along the experimental line of sight setup, the model returns the radiance for each line of sight. Through the iterative update of the input electron temperatures and densities, the difference between the calculated and measured intensity profiles is reduced, leading to converging profiles. This way, radial electron temperature and density profiles are reconstructed. The profiles are mapped along the normalized magnetic flux coordinate ρ_{pol}, requiring temporally constant profiles over the propagation time of the helium. In addition to the dynamic state populations, the model includes the reabsorption of self-emitted radiation, which is discarded in the extension described later.

III. MODIFIED CRM AND SYNTHETIC FILAMENTS

A. Changes to the CRM

The dynamic collisional radiative model, described in Sec. II and in more detail in Ref. 27, reconstructs one-dimensional radial edge profiles for the electron temperature and density over the flux coordinate ρ_{pol}. The extended version of this model for the filament analysis described in the following makes use of a three-dimensional Cartesian coordinate system, which is necessary to measure two dimensional temperatures and densities. The introduced coordinate system is indexed by "bco" for beam coordinate system, and the geometry is displayed in Fig. 1. The beam coordinate system has its origin in the injection point, with the z_{bco} vector pointing in the direction of the helium injection. z_{bco} is approximately anti-parallel to the minor radius coordinate of the plasma. x_{bco} is parallel to the central line of sight and approximately parallel to a magnetic field line for standard AUG equilibria at the position of the helium cloud. (As mentioned in Sec. II, the angle for the given equilibrium is up to 9°.) The third Cartesian axis y_{bco} is orientated binormal to the two other axis and approximately equal to the poloidal direction. Temperatures and densities are given in the z_{bco}–y_{bco} plane, with the projection in the third dimension being performed along the magnetic field line. This is important for filaments, as they are only a local perturbation in the 2D

04 November 2026 08:21:20

© Author(s) 2023

plane perpendicular to the magnetic field, but in the three dimensions, they possess a curved shape, which can be seen in Fig. 2. The implicit assumption from this is that the filament has a constant temperature and density along the magnetic field line. The projection of this curved shape in the z_{bco}–y_{bco} plane is displayed in Fig. 19, showing that no magnetic field line touches multiple lines of sight.

In the model, the temperatures and densities are given for spatial coordinates inside a cone, and the half-opening angle of the coordinate grid goes up to 40°, twice the half-opening 1/e angle of the valve.[30] After calculating the radiances of the four helium lines inside the three dimensional cone, the line integrated radiance per LOS is inferred by using the intersection points with the lines of sight. The basic geometries are displayed in Fig. 1.

In addition to the extended coordinate systems used for the evaluation, the extension of the model differs from the original model in another point. Due to the increased complexity of the geometry, the reabsorption can no longer be included. This is justified by the low injection rates for the used discharges (below 5×10^{19} s^{-1} for all measurements) and the evaluation at the 2D grid LOS, which is distant from the injection point.[27]

B. Creating synthetic filaments

For the simulation of synthetic filaments and the subsequent reconstruction of experimental filaments, various assumptions are made. The main assumption is that the electron temperatures and densities consist of a constant background profile ($T_{e,bg}$ and $n_{e,bg}$), that is perturbed by a filament. The two dimensional background is constructed by mapping the measured 1D-profiles along ρ_{pol} from the dynamic model to the 2D plane. In the discharges selected for this paper, discarding the filament time points makes no difference to the averaged background profiles, as shown in Sec. 4 of Appendix.

As there are so far no measurements of the filament temperature and density distributions, different assumptions are made. For the perturbation, it is assumed that the position of the temperature and density perturbation are identical. The perturbation, associated with a filament, is parameterized by a two-dimensional Gaussian distribution function leading to a circular cross section in the z_{bco}–y_{bco} plane. The Gaussian is determined by a 1/e width r_{fil} that is equal for the temperature and density and an amplitude factor that is multiplied to the Gaussian, which has a maximum amplitude of 1. For the temperature perturbation of the filament, an amplitude $T_{e,fil}$ is chosen for the Gaussian distribution, and analogously for the density perturbation an amplitude of $n_{e,fil}$. The resulting 2D temperature and density profiles result from the sum of the background value and the filament value: $n_e = n_{e,bg} + n_{e,fil}$ and $T_e = T_{e,bg} + T_{e,fil}$. An example of such a composition for the density can be seen in Fig. 4 in 1D (on the central injection axis). As the atomic data for the THB are calculated for Maxwellian distributions,[31] this sum of background and filament implies that the new temperature is close to a Maxwellian distribution as well, which is sometimes not the case in the SOL, for example at high densities.[32,33]

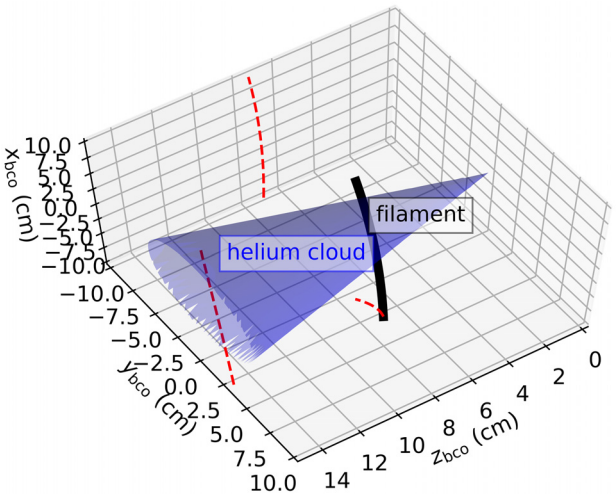


FIG. 2. Visualization of a field aligned filament with respect to the helium cloud. The same field aligned mapping is used for all points in the projection plane. The red lines are the projections of the filament on the planes.

C. Line of sight setup

For the setup at ASDEX Upgrade, a part of the LOS are placed in a 2D grid (5×5), which is spaced in average by 6 mm, having a focal spot size of 3 mm on each LOS. To visualize the intensities for synthetic and measured filaments, a 2D intensity or its perturbation is linearly interpolated between the LOS.

As the pixel density of the 2D grid is sparse, it is important to rule out the possibility that the interpolation leaves out important features in the intensity frame. To investigate this, the experimental setup for the LOS is compared with a denser artificial setup (1.2×10^6 LOS) for identical filaments in Fig. 3.

It can be seen that the main characteristics of the 2D appearance, like the position and size, remain the same in both representations. The difference between the filament position and the intensity perturbation is discussed in Sec. IV.

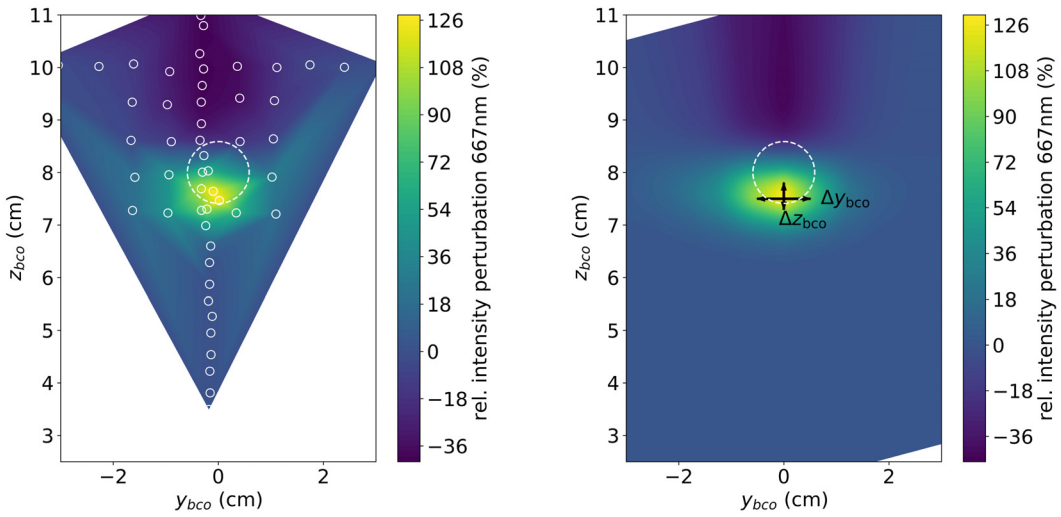
IV. SENSITIVITY ANALYSIS

Using the experimental setup for the lines of sight, synthetic filaments are simulated. As described in Sec. III B, the input electron temperatures and densities consist of the sum of the background and the filament. To determine the diagnostic capabilities to measure filaments, the parameters for the filament and background are systematically scanned. For different filament positions relative to the separatrix position, the sensitivity with regard to a constant filament amplitude is determined. In addition to this, synthetic intensities are calculated for filaments varying in size and in temperature and density amplitudes. Analogous to the measurement, the four line intensities and line ratios calculated from these transitions are used to evaluate the synthetic filaments.

The parameter range for the filaments is huge, since the background profiles, the position in the 2D grid, the size, and the filament amplitudes are varied. Therefore, only selected dependencies are shown, and the general trends are discussed. The background profiles originate from the L-mode discharge #37021, averaged over the interval from 2.2 to 3.9 s. Unless stated otherwise, the filament is given by $T_{e,fil} = 40$ eV, $n_{e,fil} = 6 \cdot 10^{18}$ m^{-3}, $z_{bco,fil} = 8$ cm, $y_{bco,fil} = 0$ cm, and $r_{fil} = 0.5$ cm. The resulting intensity differences caused by this filament are displayed in Fig. 3.

04 November 2026 08:21:20

© Author(s) 2023



(a) Experimental LOS setup

(b) Artificial LOS setup (1.2 million LOS)

FIG. 3. The relative intensity difference of the 667 nm line caused by an artificial filament, indicated by the white dashed circle, is displayed on the y_{bco}–z_{bco} plane of the beam coordinate system. In both cases, the maximum intensity perturbation amplitude is offset toward lower z_{bco} and the shape is elliptical. For higher z_{bco} values (radially further inside), the filament causes a negative intensity perturbation, which is the result of a higher ionization at the filament position. Δz_{bco} and Δy_{bco} indicate the full width half maximum (FWHM) of the intensity perturbation along the respective axis. (a) Experimental LOS setup and (b) artificial LOS setup (1.2×10^6 LOS).

A. General trends

Adding a filament to a given background leads to a positive intensity perturbation, followed by a negative intensity perturbation radially inside. The position of the positive intensity perturbation and the filament position are not necessarily identical. Following the helium injection direction, the filament causes a negative intensity perturbation, caused by the increase in the ionization through the filament, radially inside (higher z_{bco}) the positive perturbation, also observed at the lithium beam diagnostic,[34] where the position of the maximum perturbation is different due to different injection velocities.

An example of the intensity perturbation by a filament for the THB can be seen in Fig. 3 (positive intensity perturbation before the maxima of the density perturbation and negative intensity perturbation radially inside/at higher z_{bco}). For filaments in the far scrape-off layer, the positions and shapes of the input filament and the intensity response are very similar. However, the radial position of the intensity maxima is further outside than the filament position, if the filament is placed close to the separatrix, which is in most cases also the position of the intensity maximum. This effect is observed in other studies as well, for example in D_α simulations[35,36] and other experiments with different edge parameters.[14] For certain conditions, the displacement along the beam axis can be up to 1 cm, while the almost circular intensity shape becomes further inside more elliptical [see Fig. 3(b)] and can even show a half-moon shape in the 2D plane.

The comparison between the density n_e and the 667 nm intensity for profiles with and without filaments can be seen in Fig. 4(a). The figure shows a clear displacement of the $I_{667\,nm}$ perturbation further outward with respect to the density perturbation (lower values of z_{bco} correspond to radially further outward regions), as well as different relative amplitudes of density (196%) and intensity (127%) of the filament.

As the intensity is no sufficient measure for the filament position and size, the question arises whether line ratios from different transitions can be considered, which reproduce the behavior of the density perturbation. In the static model, briefly described in Sec. II, line ratios are formed.[29] By dividing the 667 nm line through the 728 nm line, a dominantly density sensitive line ratio, $R_{ne} = \frac{I_{667}}{I_{728}}$, is obtained (see also Appendix, Fig. 17). As shown in Fig. 4(b), the line ratio is capable of reproducing the shape of the density perturbation. Choosing other line ratios leads to similar results, as shown in.[37] This raises the question, whether the static model would be applicable for the calculation of filament densities and temperatures. However, due to the relative steep rise in the density and temperature profiles due to the added filament, the condition for a collisional radiative equilibrium is no longer fulfilled. As a result, the static model systematically underestimates the temperature and deviates for the electron density as well. For this paper, line ratios will be used to get an estimate for the filament position, while the collisional radiative modeling is solely performed with the extended forward model.

As stated previously, the THB at ASDEX Upgrade measures four transitions, the 667 and 728 nm lines from the singlet spin system and the 587 and 706 nm triplet transitions. For lines from the same spin system, the behavior with respect to the temperature and density is identical, and the lines only differ in the relative amplitude change. For one singlet and one triplet line, the dependency on the filament temperature and density is discussed in Sec. IV B and in Fig. 5.

B. Dependency on the temperature and density amplitude

Filaments are characterized by positive density and temperature perturbations. As the positions of the filament and intensity

04 November 2026 08:21:20

© Author(s) 2023

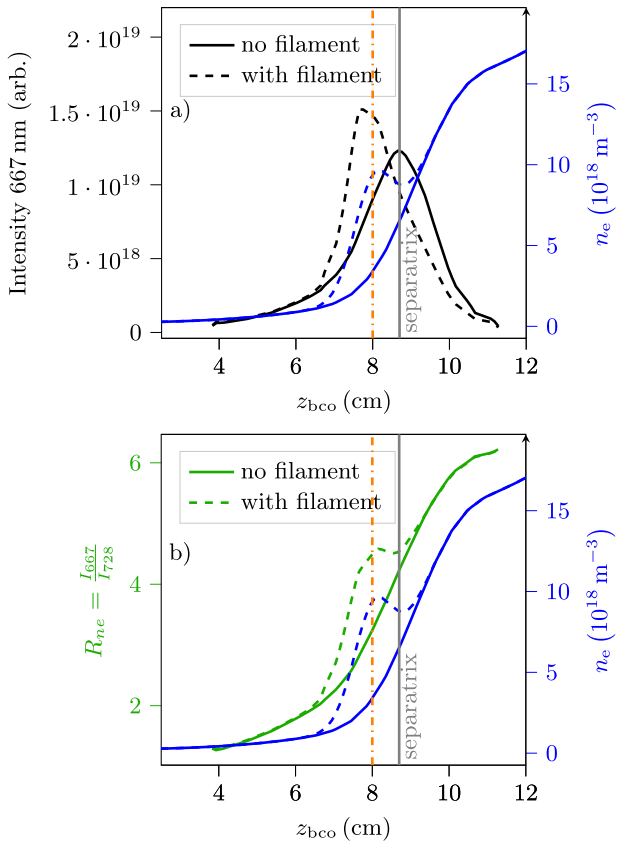


FIG. 4. One dimensional cut through $y_{bco} = 0$ for the artificial filament displayed in Fig. 3. In blue, the density background is displayed with a solid line, the profile with filament is displayed by a dashed line. In subplot (a), the same cuts for the 667 nm emission are displayed, while subplot (b) shows the density sensitive line ratio. The vertical orange line indicates the filament position.

perturbation are not identical, we compare the maximum of the intensity perturbation with the filament amplitude.

In Fig. 5, the dependency of the intensity perturbation on $T_{e,fil}$ and $n_{e,fil}$ is displayed for two different helium lines. For both transitions, the intensity perturbation is dominantly influenced by the filament density. The filament temperature $T_{e,fil}$ causes only minor corrections to the intensity change $\frac{\Delta I}{I}$, leading to the fact that the different lines in the figures for the temperature sensitivity are vertically spaced by their different densities $n_{e,fil}$. Differences between the two spin systems are clearly visible in the temperature sensitivity. The triplet system with the 587 nm line has a relative population maximum at 25 eV. As the background temperature at the filament position is already 55.9 eV, the intensity of the 587 nm line drops for the entire range of added filament temperatures. In contrast to this, the singlet transition 667 nm has a monotonic but flattening rise with the temperature.

A similar analysis for the line ratios is shown in Fig. 6. For this purpose, the change of the line ratio is divided by the background line ratio, and analogous to the previous figures, the maximum change of the line ratio is determined. They are labeled R_{Te} and R_{ne} according to their dominant dependency. The temperature dependent line ratio $R_{Te} = \frac{I_{728}}{I_{706}}$ shows a nearly linear dependency on the temperature, which is displayed in Fig. 6(b). The offset and slope of this correlation have a dependency on the density $n_{e,fil}$. For the density sensitive line ratio $R_{ne} = \frac{I_{667}}{I_{728}}$, the dependency on the blob density $n_{e,fil}$ is displayed in Fig. 6(a). Its curve shape is similar to the raw emission changes along the density, showing no strong difference caused by $T_{e,fil}$.

C. Relation between the intensity size and temperature and density size of the filament

The filaments in the density picture differ from the measured intensity perturbation in multiple points. It is important to understand the exact relationship between the two images, since sometimes the assumption is made that one can set the relative perturbations in both quantities equal.[12] As described previously, the position between both perturbation maxima differs as well as the shape and size of the perturbation, the latter being discussed in more detail here.

The intensity size is determined along the two axes of the beam coordinate system. Δz_{bco} is determined by fitting a Gaussian on the relative intensity perturbation cross section along z_{bco}, which goes through the maximum intensity. Δz_{bco} is the FWHM of this Gaussian. The analog procedure is performed to get Δy_{bco}, which is displayed in Fig. 3(b). Both values are compared against the input filament size, equal for $T_{e,fil}$ and $n_{e,fil}$, which determines the width of the Gaussian filament. The amplitude of the Gaussian, i.e., the amplitude of the filament, is kept constant over the scan, as well as the background profile, which has at the filament center values of $T_{e,bg} = 55.9$ eV and $n_{e,bg} = 3.6 \times 10^{18}$ m^{-3}.

In Fig. 7, the relation between the filament width and the resulting size in the intensity frame is shown. For filament widths below 2 mm, the LOS setup prevents a meaningful evaluation (LOS spacing is 6 mm), while input widths of the filament increase the ellipticity of the intensity response. This can be seen by the increase in the ratio between Δy_{bco} and Δz_{bco}, i.e., the poloidal width of the intensity perturbation increases more strongly than the radial width.

For filaments with a given size of 1.4 cm, the FWHM of the resulting intensity perturbation along the y_{bco} axis is 2.4 cm, which corresponds to the size of the 5×5 grid, setting a hard limit for the maximum useful intensity size of the filament. Remarkably, the apparent radial width of the filament, estimated as z_{bco}, is smaller than the width of the density for the given inputs. Therefore, the filaments appear smaller than they actually are. The reason is the increased ionization, which causes an neutral helium and intensity drop further radially inside, resulting in a smaller appearance of the intensity perturbation. This effect also causes the increased ellipticity of the intensity perturbation with an increased filament size. Even for the smallest sizes, the circular density and temperature perturbation cause an elliptical intensity perturbation.

In addition to exceeding the 5×5 grid, large filaments shift the position of the intensity maxima, for the fixed density position in this comparison, radially further outward (corresponding to smaller z_{bco} values), which further hinders a meaningful evaluation.

It can be seen that there is no linear correlation between both quantities, and the intensity size is up to two times larger than the density one. This case contradicts the general interpretation, which is sometimes made for GPI, that the sizes and fluctuation amplitudes between intensity and density are similar.[12]

04 November 2026 08:21:20

© Author(s) 2023

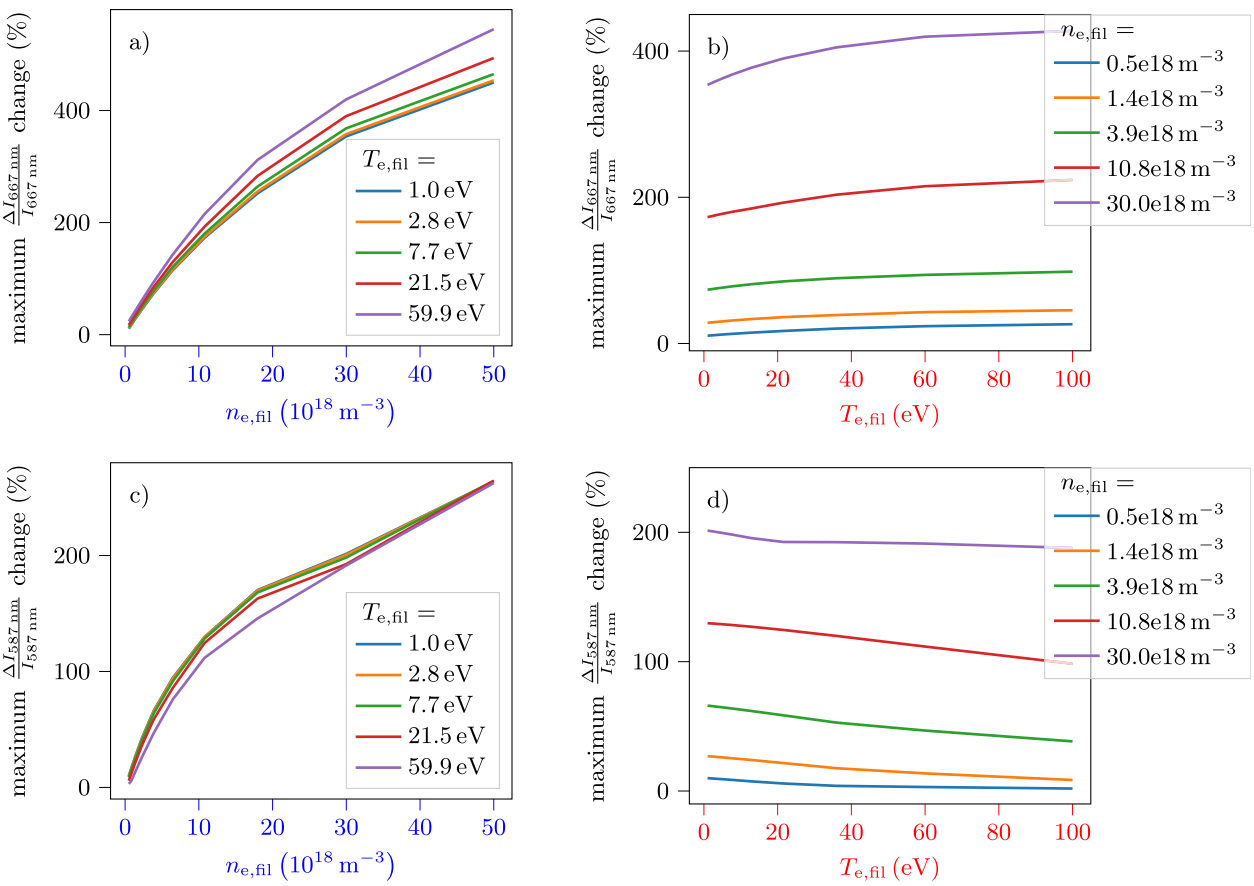


FIG. 5. The maximum relative intensity change of the 667 and 587 nm line depending on the given filament temperature $T_{\mathrm{e,fil}}$ and density $n_{\mathrm{e,fil}}$.

D. Sensitivity to shifted background profiles

As stated in Sec. IV B, with the temperature and density dependency, the intensity change is a combination of the filament amplitudes and the background temperature and density. To simulate a possible shift of the plasma equilibrium with respect to the line of sight positions, the background profiles are moved along the z_{bco} axis. In contrast to shifting the filament position, this method prevents the influence of other factors, as the distance between the valve and the filament is always constant and the filament is always located at the identical position with respect to the lines of sight. This is identical to the experiment shifting the magnetic equilibrium against the fixed lines of sight. To visualize the shift, the separatrix is indicated, but the main influence comes from the density profile, which forms the shape of the emission profile.

In Fig. 8, the density profile of Fig. 4(a) is shifted by +2.5 cm [Fig. 8(a)] and −2.5 cm [Fig. 8(b)]. As a result, the total intensity profile and the perturbation of the intensity change significantly. The case with the positive shift corresponds to shifting the separatrix away from the valve, placing the 5 × 5 grid further outside in the SOL. Here, the position of the filament and the intensity perturbation are nearly identical. Due to the low helium line excitation, caused by low background temperatures and densities, the filament makes a significant perturbation, causing a tenfold of the 667 nm intensity. As a result, the intensity curve with the filament has two peaks, one at the filament position and the other one caused by the background profiles further inside.

Shifting the profile by 2.5 cm in the negative direction corresponds to placing the filament in the confined region. The response is in this case very small on the intensity curve, as the filament position is behind the intensity peak, i.e., further inside the plasma. In a narrow range between 6 and 7.5 cm, the filament causes a tiny positive intensity perturbation, displaced from the filament position at 8 cm. For $z_{\mathrm{bco}} > 8$ cm, the intensity drops, causing a clear separation between the position of the maximum intensity perturbation and the filament position. The maximum relative intensity perturbation is only 4.5%.

By consecutively shifting the background profile between the two discussed cases, Fig. 9 is created. The logarithmic representation reveals that the relative intensity perturbation by the filament is maximized in the far SOL, causing strong changes in relative intensity by small shift of the background profiles. Overall, this curve is almost linear in the logarithmic representation indicating that the relative intensity response of a filament with a given fixed density and temperature amplitude decreases exponentially for outward shifted background profiles.

As the diagnostic has intrinsic fluctuations caused by photon noise and electronic components, which add up to the passive background fluctuations by the plasma, the very low intensity change near

04 November 2026 08:21:20

© Author(s) 2023

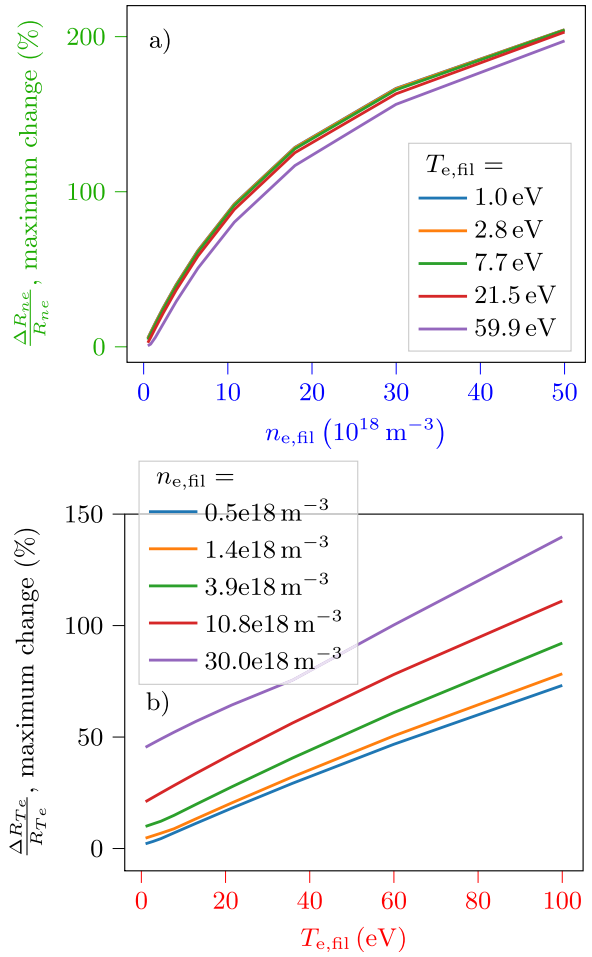


FIG. 6. Normalized line ratio difference (with and without filament) vs filament amplitude for (a) density ($R_{ne} = \frac{I_{667}}{I_{728}}$) and (b) temperature ($R_{Te} = \frac{I_{728}}{I_{706}}$). In comparison with the intensities in Fig. 5, the R_{T_e} line ratio has a dominant temperature dependency.

the separatrix by adding a filament to the background places a limit for the measurement capabilities. Due to the combination of different effects, no general criterion for the ability to detect filaments with given amplitudes can be defined. However, as a rule of thumb, equilibria with the separatrix position far inside are recommended due to the high relative intensity changes by the filament. This restriction of the measurement region, preferring filament measurements in the far SOL, applies similarly to GPI.[10,12]

E. Reconstruction of synthetic filament properties

The reconstruction algorithm makes use of a combination of a Gaussian process regression (GPR)[38] and a gradient descent optimization. The GPR is used to get close to the minima of the cost function, while the final optimization is performed with a gradient descent algorithm.

As described in the previous parts, the density sensitive line ratio fits the perturbation shape best and is used to determine the initial

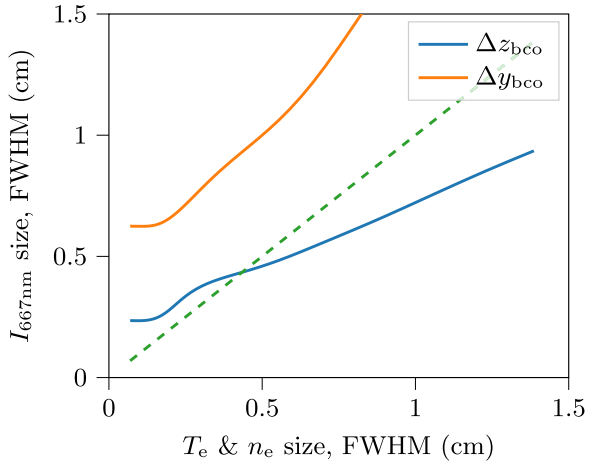


FIG. 7. Intensity vs input filament size (FWHM). The relation is non-linear, at small scales due to the limited number of LOS and at large scales due to increasing ellipticity caused by the stronger increase in Δy_{bco}.

position of the underlying electron temperature and density perturbation. This initial guess is used to set boundaries for the position reconstruction. By optimizing the 2D position together with the filament width and the electron temperature and density amplitude, the given

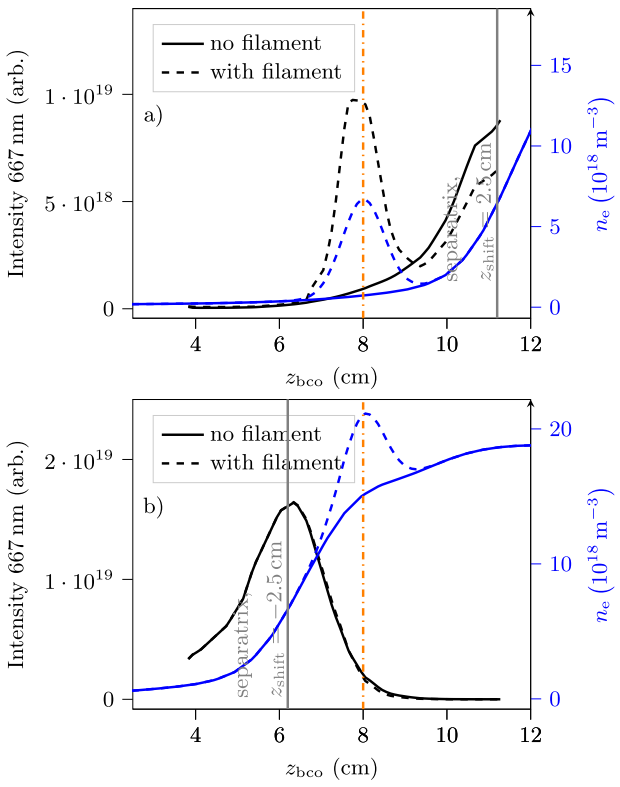


FIG. 8. Influence of shifted background profiles on the filament induced intensity response. The perturbation caused by the filament in panel (b), in positive and negative direction, is tiny and therefore hardly visible.

04 November 2026 08:21:20

© Author(s) 2023

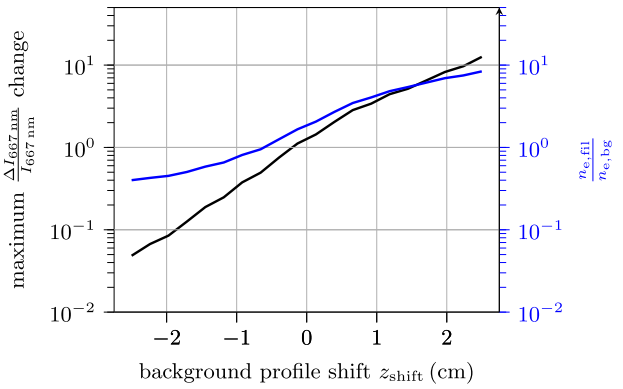


FIG. 9. Maximum relative intensity perturbation of the 667 nm line for a background shift along the z_{bco} axis. On the right axis, the ratio between the constant filament density and the varying background density is displayed. Positive z_{shift} values correspond to the displacement of the filament in the direction of the far-SOL, while negative values describe a displacement in the direction of the confined region.

synthetic or experimental filament is reconstructed by minimizing the cost function. This cost function consists, as in the profile reconstruction,[27] of the 587 nm intensity and the $\frac{I_{728\,\mathrm{nm}}}{I_{587\,\mathrm{nm}}}$, $\frac{I_{667\,\mathrm{nm}}}{I_{728\,\mathrm{nm}}}$, and $\frac{I_{728\,\mathrm{nm}}}{I_{706\,\mathrm{nm}}}$ line ratios and is only applied to the LOS in the 5×5 grid.

In preparation for the reconstruction of experimental filaments, the intensities of synthetic filaments are handed to the reconstruction algorithm, and the data are used to determine the correct reconstruction. This reconstruction is used as a test bed to determine the reconstruction capabilities. Table I compares the reconstructed filament parameters from their input values.

Because of the discrete spacing of the lines of sight, the largest deviations are on the filament size, which also affects the filament amplitudes and slightly the position. The position is recovered much better than the filament amplitudes, as the intensity amplitude is highly sensitive to the background profiles. When comparing the case with and without noise, it is found that the reconstruction gets worse for the temperature amplitude, which is not fully captured in its uncertainty.

V. RECONSTRUCTION OF EXPERIMENTAL DATA

To visually clearly distinguish whether synthetic or measured intensity maps of filaments are displayed, the measured filaments are shown in the poloidal cross section of AUG. A comparison between both coordinates can be seen in Fig. 1. The reconstruction runs for the synthetic and measured filaments solely on the measurement points of the 5×5 grid. Due to some hardware failure, one line of sight in the 5×5 grid could not be used for the presented experimental data. The setup can be seen in Fig. 12, where the LOS is missing in the upper right corner of the central 3×3 grid.

TABLE I. Results of the synthetic filament reconstruction.

	Input	Reconstruction (no noise)	Reconstruction (10% random noise)
$T_{e,fil}$	20.0 eV	19.69 eV	(10.6 ± 3.3) eV
$n_{e,fil}$	$2.0 \cdot 10^{18}$ m^{-3}	$1.94 \cdot 10^{18}$ m^{-3}	$(2.1 \pm 0.1) \cdot 10^{18}$ m^{-3}
r_{fil}	0.27 cm	0.36 cm	(0.35 ± 0.02) cm
z_{bco}	8.5 cm	8.50 cm	(8.57 ± 0.03) cm
y_{bco}	0.0 cm	−0.01 cm	(-0.10 ± 0.03) cm

A. Conditional averaging the signal

For the experimental evaluation, the I-phase[39–41] discharge #40425 is chosen. The plasma current is 800 kA, the discharge is heated with 840 kW ECRH and has a line integrated edge density of 2.5×10^{19} m^{-2}, the toroidal field strength is 2.5 T, and the safety factor is $q_{95} = 4.8$. As discussed previously in Sec. IV D, the separatrix is placed radially inside compared with an usual magnetic equilibrium, to a position of a major radius of $R_{maj} = 2.09$ m. This allows to measure the filaments in the scrape-off layer. (The position of the flux surfaces with respect to the grid can be seen in Fig. 12.) The averaged background profile of the interval from 4.78 to 5.78 s, calculated by the THB, is displayed in Fig. 10.

For ASDEX Upgrade, the threshold for a perturbation to be identified as a filament is defined to be 2.5σ corresponding to 2.5 standard deviations away from the mean. The choice of the threshold slightly varies for different tokamaks.[42–45] This criterion is applied to the measured intensity of the 667 nm transition at the center LOS in the grid ($\rho_{pol} = 1.06$). The time trace of the intensity is displayed in Fig. 11, where the signal is smoothed over seven time points, and afterward, the criterion is applied.

In the first step, all intervals with one or multiple time points above the 2.5σ values are determined. For each of these intervals, the trigger time point ($\Delta t = 0$) is now selected as the time point with the maximum intensity. In addition, an upper limit is set at 10σ, discarding the time point if its maximum intensity is more than 10 standard deviations away from the mean. This is done to get more similar filaments and exclude very large transients. As only 11 filaments have an amplitude above 10σ, the influence of adding them to the averaging is weak, which in the end marginally affects the outcome of the reconstruction steps.

Evaluating individual filaments is often limited by the low signal to noise ratio. As a consequence, the reconstruction is not very robust.

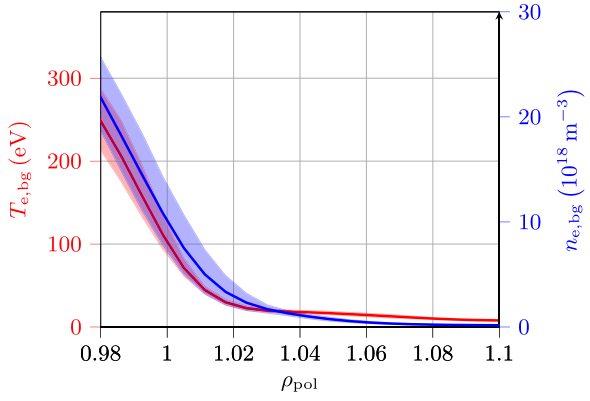


FIG. 10. Discharge #40425: background profiles for temperature and density over the coordinate ρ_{pol}. The opaque area corresponds to the standard deviation of the profile.

04 November 2026 08:21:20

© Author(s) 2023

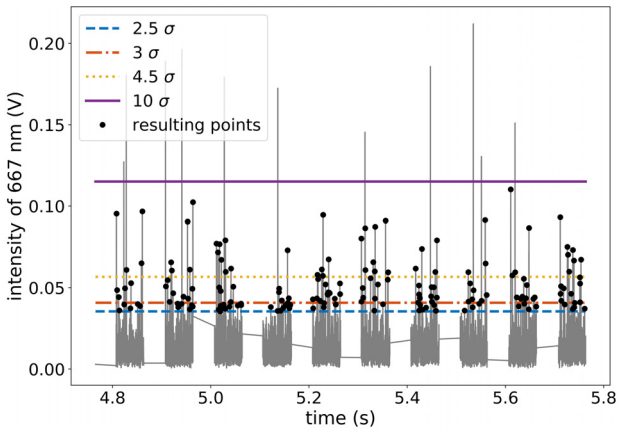


FIG. 11. Signal of the 667 nm intensity at the central LOS for discharge #40425. In the first part, the entire interval from $2.5-10\sigma$ is used. For each time interval within this threshold, the time point of maximum intensity, indicated by black circles, is selected as the filament trigger time point.

Therefore, conditional averaging is used for the presented analysis to evaluate the 174 remaining filaments (filament frequency $f_{\text{fil}} = 290$ Hz).[46,47]

B. Reconstructing the filament at the experimental time point

Since the filament is not clearly visible in the 2D raw emission, the background is subtracted, analogous as done for GPI.[12] Figure 12 shows the perturbation of the conditionally averaged 667 nm intensity at $\Delta t = 0\ \mu$s, created by subtracting the background intensity and normalizing to the background. For the other singlet line 728 nm, the perturbation looks similar, while the perturbation for the triplet transitions (706 and 587 nm) is slightly shifted radial outward (not shown in the paper).

C. Results of the experimental reconstruction

In Table II, the parameters of the reconstruction are displayed. The relative temperature perturbation by the filament is $\frac{T_{e,\text{fil}}}{T_{e,\text{bg}}} = 84\,\%$, and the density perturbation is $\frac{n_{e,\text{fil}}}{n_{e,\text{bg}}} = 73\,\%$. Similar to synthetic filaments, in the experiment the position of the filament is radially further inside, compared to the intensity perturbation, which is displayed in Fig. 13(c). The cross indicates the position of the filament, while the filled circle is the position of the center of mass, calculated from the intensity perturbation. Analogous to the maximum position of the perturbation, the center of mass is radially further outside (corresponds on the low field side to a larger radius R). The position of the filament is slightly shifted in the z-direction.

TABLE II. Results of the filament reconstruction. The filament corresponds to the conditional averaging, evaluated at $\Delta t = 0\ \mu$s. The background values are $T_{e,\text{bg}} = 14.9$ eV and $n_{e,\text{bg}} = 1.5 \times 10^{18}$ m^{-3}.

$T_{e,\text{fil}}$	=	(13 ± 7) eV
$n_{e,\text{fil}}$	=	$(1.1\pm0.3) \times 10^{18}$ m^{-3}
r_{fil}	=	(0.9 ± 0.1) cm
$z_{\text{bco,fil}}$	=	(9.1 ± 0.2) cm
$y_{\text{bco,fil}}$	=	(0.07 ± 0.24) cm
$\text{width}_{\text{fil,FWHM}}$	=	2.37 cm
R_{fil}	=	2.10 m
z_{fil}	=	-0.135 m

The optimization leads to a stable minimum, showing that the selected amount of optimization parameters is enough to reconstruct the measurement. The reconstructed line ratios and intensity are presented in Sec. 5 of Appendix. The correlation of three optimization parameters is displayed in Fig. 26.

VI. COOL DOWN OF FILAMENTS IN THE FAR SOL

The evolution of the conditionally averaged filament is shown in Fig. 13. Analogous to the displayed reconstruction at $\Delta t = 0\ \mu$s in Sec. V, the reconstruction algorithm evaluates the four other time steps. The reconstructed filament positions are indicated as the purple crosses in the different timesteps of Fig. 13, while the temporal evolution of the other three quantities (T_e, n_e, r_{fil}) is displayed in Fig. 14.

In Fig. 14(a), the total temperature and density of the filament determined at the reconstructed center, i.e., in the co-moving frame of

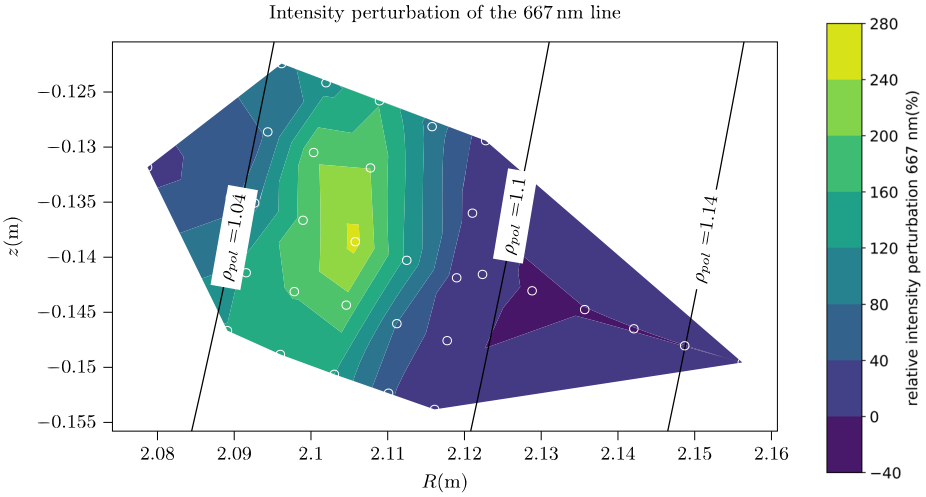


FIG. 12. The conditionally averaged (2.5σ–10σ) 667 nm intensity perturbation $\frac{I-\bar{I}}{\bar{I}}$ at the trigger time point $\Delta t = 0$ of discharge #40425. For triggering, the central line of sight is used, located in the center of the 5×5 grid. The white circle indicates the position of lines of sight available during the experiment. The negative intensity perturbation around $R = 2.13$ m comes from a temporal fluctuation, while the negative intensity difference at $R = 2.08$ m comes from the neutral helium ionization caused by the filament.

04 November 2026 08:21:20

© Author(s) 2023

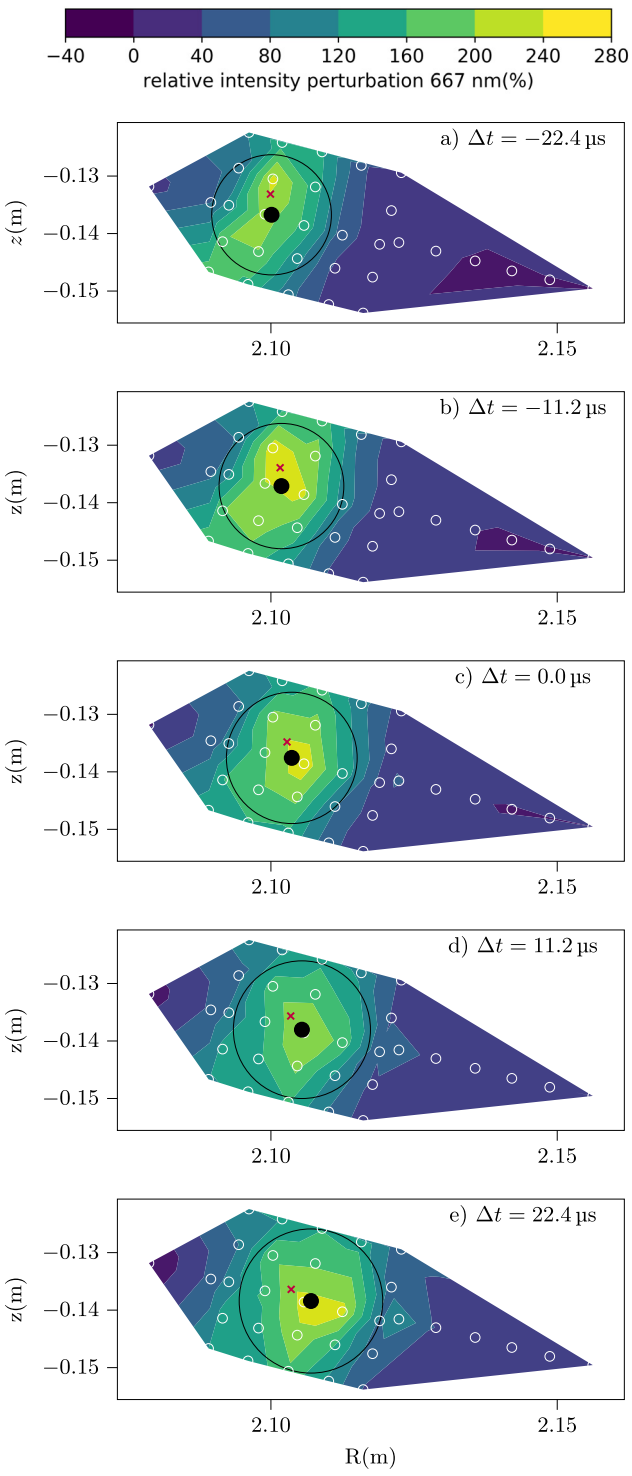


FIG. 13. Time trace of the 667 nm intensity perturbation from the conditionally averaged signal ($2.5\sigma - 10\sigma$). The white circles indicate the LOS positions, the black point and line indicate the intensity center of mass $\bar{\mu}$ and variance σ_{int}, while the purple cross indicates the reconstructed position (R_{fil}, z_{fil}).

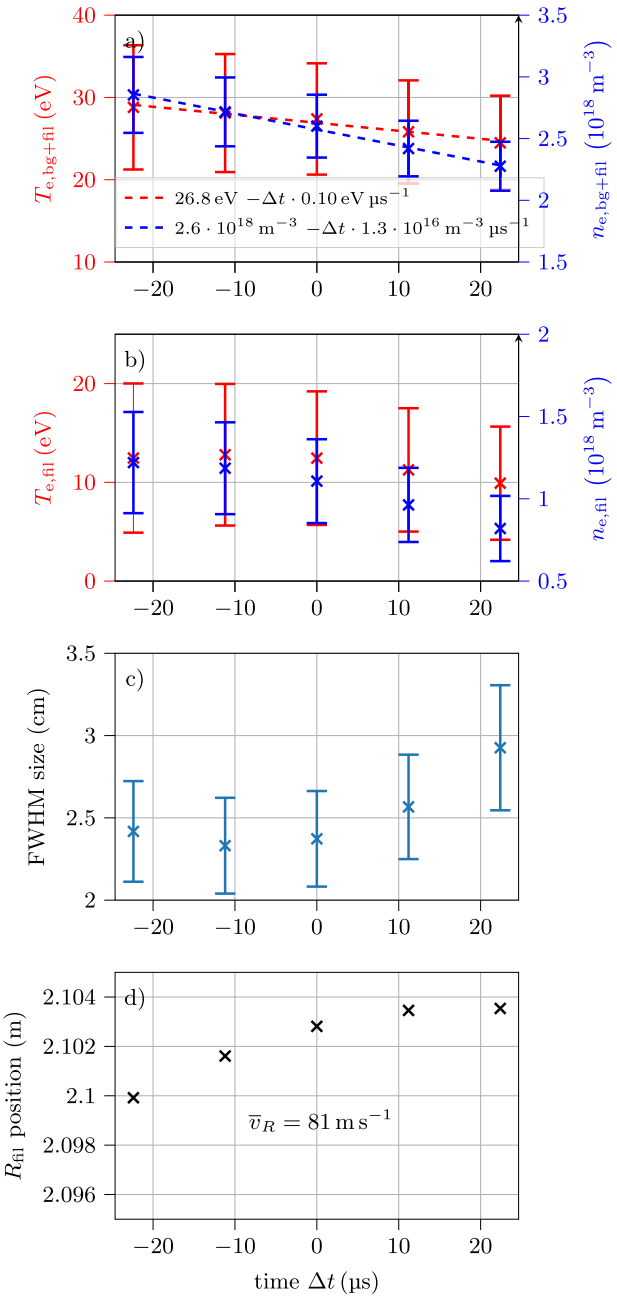


FIG. 14. The figure shows the reconstructed filament properties (of filaments between 2.5σ and 10σ) in subplots (b)–(d). All properties are in the co-moving frame, showing the properties at the center of the filament. In subplot (a), the sum of the background and filament amplitude are displayed for temperature and density. Through both values, a linear regression is made.

the filament, are shown over time, with the trigger time point at $\Delta t = 0\,\mu s$. The trigger time point comes from the overlay of the conditional averaging. In order to estimate an average loss rate, a linear fit is performed, leading to decay rates of 0.10 eV μs^{-1} and 1.3×10^{16} m^{-3} μs^{-1}. The decay of temperature and density in Fig. 14(a) consist of two

04 November 2026 08:21:20

© Author(s) 2023

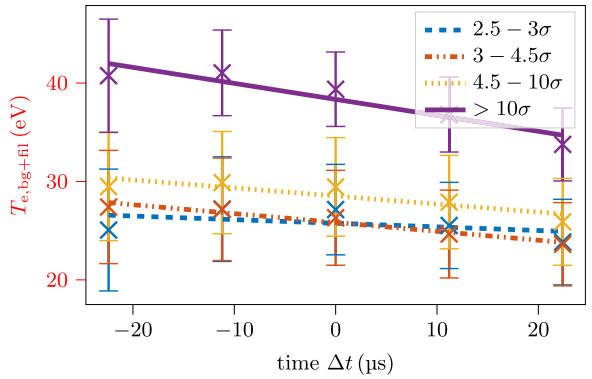


FIG. 15. The filament temperature in the co-moving frame for multiple intensity resolved sup-intervals of the 667 nm line. Through each time trace, a linear regression is performed; its values can be found in Table III.

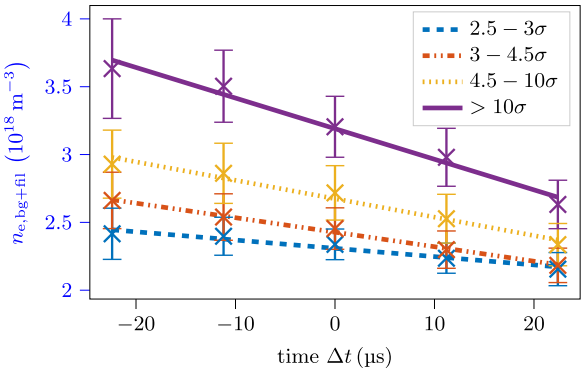


FIG. 16. The filament density in the co-moving frame for multiple intensity resolved sup-intervals of the 667 nm line. Through each time trace, a linear regression is performed; its values can be found in Table III.

parts. On the one side, the background value decreases by the filament propagating outward. Conversely, the filament amplitude ($T_{e,fil}$ and $n_{e,fil}$) decreases as well over time, which is displayed in Fig. 14(b).

Figure 14(c) shows the evolution of the filament size, represented by the full width half maximum (FWHM) size. As a result of the conditional averaging, a parabolic curve is expected. This is caused by the velocity distribution of the individual filaments (as showed by Ref. 2 in Fig. 6 for different scenarios and positions), which leads to a loss of spatial coherence with increasing temporal distance to the trigger point. The loss can be explained by the triggering, which captures all filaments at the same position. By progressing forth and back in time, faster filaments propagate farther than slower ones, which leads through averaging to an increased apparent size of the averaged filament. The reconstruction leads to the expected parabolic shape of the temporal evolution of the width, with the minimum being at -11.2 μs and not at the trigger time point, but still within errors. Due to this effect, the underlying physical behavior of the filaments cannot be clearly separated from the expected influence of conditional averaging, which greatly limits the interpretation of the filament width.

The effect of conditional averaging is also expected to influence the position of the reconstruction. In the last time points, it can be seen that an increase in the size goes parallel with a slowing down in the motion, seen by the decreasing radial steps in Fig. 14(d), which is also expected from the loss of spatial coherence.

To use more similar filaments for the further evaluation of temperature and density decay rates, the measurement performed for all filaments in the 2.5 to 10σ range is repeated for narrower intensity perturbation intervals. For the filaments in the intervals of 2.5–3σ (54 filaments), 3–4.5σ (74 filaments), 4.5–10σ (51 filaments), and $>10\sigma$ (11 filaments), the filament parameters are reconstructed as previously for the wider sigma range (for the intensity intervals, see Fig. 11). In each of the intensity intervals, a linear regression is performed on the temperature and density, as shown in Figs. 15 and 16. The values of the regression are written in Table III. Even though there are multiple non-linear processes involved, the temperature decay rate (-0.10 eV μs^{-1}) and temperature offset (26.8 eV) of the 2.5–10σ interval agree surprisingly with the mean decay rates (-0.10 eV μs^{-1}) and offset (26.7 eV) of the three sup-intervals (2.5–3σ, 3–4.5σ, 4.5–10σ). When averaging the density offset of the three sup-intervals, the result of 2.5×10^{18} m^{-3} is marginally lower than the offset from the entire range (2.6×10^{18} m^{-3}). The mean density decay rate of the three sup-intervals of -1.3×10^{16} m^{-3} μs^{-1} is within the errorbars equal to the decay rate of the entire intensity range.

The resulting decay rates of the sup-intervals are compared with different models. The density decays via convective transport, given by

TABLE III. The table compares the slopes of the linear regressions of n_e and T_e decay in the co-moving frame of the filament, from Figs. 15 and 16, with the decay rates predicted by different models. The different sigma intervals group filaments with similar intensity amplitudes together.

	$T_{e,bg+fil}$				$n_{e,bg+fil}$		
	Measurement		Conduction model	Sheath limited model	Measurement		Convection model
	$T_e(\Delta t=0)$ (eV)	$\frac{dT_e}{dt}\left(\frac{\text{eV}}{\mu\text{s}}\right)$	$\frac{dT_e}{dt}\left(\frac{\text{eV}}{\mu\text{s}}\right)$	$\frac{dT_e}{dt}\left(\frac{\text{eV}}{\mu\text{s}}\right)$	$n_e(\Delta t=0)\left(10^{18}\frac{1}{\text{m}^3}\right)$	$\frac{dn_e}{dt}\left(10^{16}\frac{1}{\text{m}^3\mu\text{s}}\right)$	$\frac{dn_e}{dt}\left(10^{16}\frac{1}{\text{m}^3\mu\text{s}}\right)$
$2.5\sigma-3\sigma$	25.9 ± 0.6	-0.05 ± 0.04	-0.09	-0.23	2.31 ± 0.01	-0.66 ± 0.08	-1.2
$3\sigma-4.5\sigma$	25.8 ± 0.2	-0.09 ± 0.01	-0.09	-0.23	2.43 ± 0.01	-1.1 ± 0.1	-1.2
$4.5\sigma-10\sigma$	28.5 ± 0.4	-0.09 ± 0.03	-0.11	-0.27	2.68 ± 0.02	-1.4 ± 0.1	-1.4
$>10\sigma$	38.5 ± 0.5	-0.18 ± 0.03	-0.26	-0.41	3.20 ± 0.03	-2.4 ± 0.2	-2.0

04 November 2026 08:21:20

© Author(s) 2023

Eq. (A1). For the ion sound velocity, the ion/electron temperature ratio is assumed to be $\tau_i = \frac{T_i}{T_{e,bg+fil}} = 3$, which is supported by results from AUG[48] and other tokamaks.[49] The temperature decay is calculated with Eq. (A2), while the parallel heat flow is given by either the Spitzer–Härm parallel heat conduction [Eq. (A3)][50] or the sheath limited convective transport [Eq. (A4)]. The connection length is half the length of the magnetic field line between the inner and outer divertor and passing through the central LOS, giving $L_c = 32\,\mathrm{m}$ (see also Fig. 20). The model decay rates are compared with the experimental values in Table III.

For temperature decay, the parallel conduction model best captures experimental data and agrees within the errorbars with the decay rates of the three lowest sigma intervals. Model and measurement differ only for the filaments above 10σ. A possible mechanism for this difference could be the electron-ion heat exchange. For $\tau_i = 3$ and the hottest filaments ($>10\sigma$), the cooling rate of the electrons increases only by $+0.03\,\mathrm{eV}\ \mu\mathrm{s}^{-1}$. Therefore, no definitive statement can be made on the impact of the energy exchange.

Cooling by convective losses overestimates the temperature decay rates for all sigma intervals. Since the convective heat flux is proportional to the ion sound speed, lower ion temperatures ($\tau_i < 3$) would reduce the heat flux and the cooling rate.

The convective transport captures the density decay and agrees within error with the measured decay rates of the 3–4.5σ and 4.5–10σ intervals. In contrast to the sheath limited power flux, the density decay rates support the assumption that $T_i = 3 \cdot T_e$ if the density decays by convection alone.

The experimentally measured relative temperature decay rates are between 0.2% and 0.5% $\mu\mathrm{s}^{-1}$, while the relative density decay rates are between 0.2% and 0.75% $\mu\mathrm{s}^{-1}$. This is in contrast to blob models assuming cold ions, which expect faster relative temperature decay than density decay.[51]

In summary, comparing the measured and modeled decay rates, the temperature decay is best described by conductive transport for the given discharge. In contrast, the density decay can be approximately described by convective transport. Both models have assumed $\tau_i = 3$, which supports the statement that filaments are best explained by warm ion models.[7,52]

VII. CONCLUSION AND OUTLOOK

In this work, the usage of the thermal helium beam diagnostic for filament measurements of n_e and T_e at ASDEX Upgrade is described.

By modifying a collisional radiative model, the two dimensional setup of the diagnostic was exploited. The model was used in a first step to simulate the measurement process using synthetic filaments. It was shown that the intensity perturbation mainly depends on the electron density of the filament, while the temperature plays only a minor role. In addition to this, the size, amplitude, and position of the intensity perturbation do not necessarily represent the respective values of the temperature and density perturbation. We demonstrated that the diagnostic reacts only weak to n_e and T_e fluctuations around the separatrix where the density and temperature are relatively large. Therefore, $n_{e,fil}$ and $T_{e,fil}$ at the assumed birth location of filaments cannot be investigated, while the measurements in the far SOL deliver clear results.

Using the same CRM, filament temperatures and densities were reconstructed from conditionally averaged experimental data. Conditional averaging was applied to get a high signal-to-noise ratio and needed for a successful reconstruction, bringing new potential errors in the estimation of the filament size and velocity. For the given discharge, the resulting electron temperatures and densities are over 70% higher than the background values, with both quantities decaying over time. The conditional averaged interval was divided into subintervals to better compare the decay rates with model assumptions. For the discharge, the temperature decay is best described by Spitzer–Härm parallel conduction. Under the assumption that $\tau_i = 3$, the density decay is described by convective transport. The comparison of the relative decay rates further supports the hypothesis for the ion temperature, as the relative decay rates of temperature and density are in the same order, which does not appear in cold ion models.

These measurements of the decay rates are essential to quantify and better understand the power flux deposited onto the plasma-facing components. Further studies in different plasma scenarios are envisaged to quantitatively relate the measured cooling rates to SOL power balance models and the impact of filaments on wall erosion. In addition, the decay rates shall be compared with the results of more advanced heat flow models.[53,54]

ACKNOWLEDGMENTS

This work has been carried out within the framework of the EUROfusion Consortium, funded by the European Union via the Euratom Research and Training Programme (Grant Agreement No. 101052200—EUROfusion). Views and opinions expressed are, however, those of the author(s) only and do not necessarily reflect those of the European Union or the European Commission. Neither the European Union nor the European Commission can be held responsible for them.

D. Wendler and G. Birkenmeier received funding from the Helmholtz Association under Grant No. VH-NG-1350.

AUTHOR DECLARATIONS

Conflict of Interest

The authors have no conflicts to disclose.

Author Contributions

Daniel Wendler: Conceptualization (equal); Data curation (equal); Formal analysis (equal); Investigation (equal); Software (equal); Writing – original draft (lead). **Gregor Birkenmeier:** Conceptualization (supporting); Formal analysis (supporting); Funding acquisition (equal); Investigation (supporting); Supervision (equal); Writing – original draft (supporting); Writing – review & editing (equal). **Michael Griener:** Conceptualization (supporting); Formal analysis (supporting); Investigation (supporting); Supervision (equal); Writing – original draft (supporting); Writing – review & editing (equal). **Ralph Dux:** Formal analysis (supporting); Software (supporting); Writing – review & editing (supporting). **Rainer Fischer:** Software (supporting); Validation (supporting); Writing – review & editing (supporting). **Dirk Joachim Stieglitz:** Formal analysis (supporting); Software (supporting); Validation (supporting). **Elisabeth Wolfrum:** Conceptualization (supporting); Supervision (equal); Writing – review & editing (supporting). **Ulrich Stroth:** Conceptualization (supporting); Funding acquisition (equal);

04 November 2026 08:21:20

© Author(s) 2023

Supervision (equal); Writing – review & editing (supporting). **ASDEX Upgrade Team:** Funding acquisition (equal); Resources (equal).

DATA AVAILABILITY

The data that support the findings of this study are available from the corresponding author upon reasonable request.

APPENDIX: TECHNICAL DETAILS

1. Line ratio plot for the static CRM

Line ratio grid for the static model. It is based on the theoretical photo emission coefficients. The density sensitive line ratio in black is given as $\frac{I_{667\,\mathrm{nm}}}{I_{728\,\mathrm{nm}}}$, while the temperature sensitive line ratio in red is determined from $\frac{I_{728\,\mathrm{nm}}}{I_{706\,\mathrm{nm}}}$. By forming the line ratio from the experimental data, temperatures and densities can be calculated by determining the intersection point in the atomic data grid.

2. Resolution of the grid

To determine the resolution of the THB setup at AUG, the angle between the LOS and the magnetic field line is calculated. In Fig. 18, it can be seen that this angle is for the entire grid in the range of 6° to 9°. As the magnetic field lines, as well as the lines of sight, are nearly perpendicular to the z_{bco}–y_{bco} plane, the projection of the magnetic field lines in this plane is displayed in Fig. 19 for each LOS. The figure shows that the magnetic field lines do not touch multiple LOS, wherefore the intensity on each LOS origins from a single magnetic field line. This affects only the perception in the intensity picture, as the magnetic field geometry is fully implemented in the extended forward model for the temperature and density.

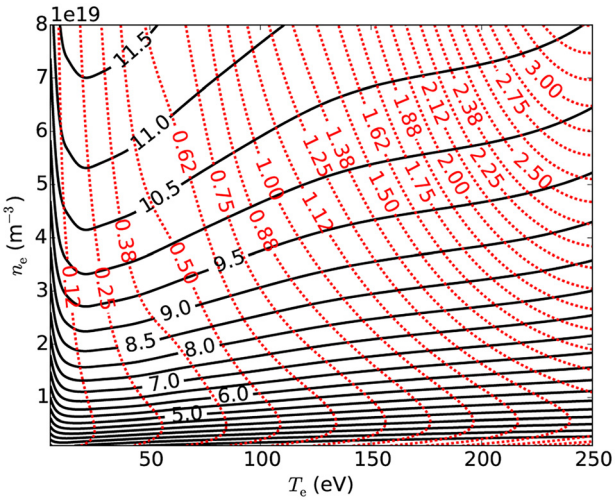


FIG. 17. Line ratio grid for the static model. It is based on the theoretical photo emission coefficients. The density sensitive line ratio in black is given as $\frac{I_{667\,\mathrm{nm}}}{I_{728\,\mathrm{nm}}}$, while the temperature sensitive line ratio in red is determined from $\frac{I_{728\,\mathrm{nm}}}{I_{706\,\mathrm{nm}}}$. By forming the line ratio from the experimental data, temperatures and densities can be calculated by determining the intersection point in the atomic data grid.

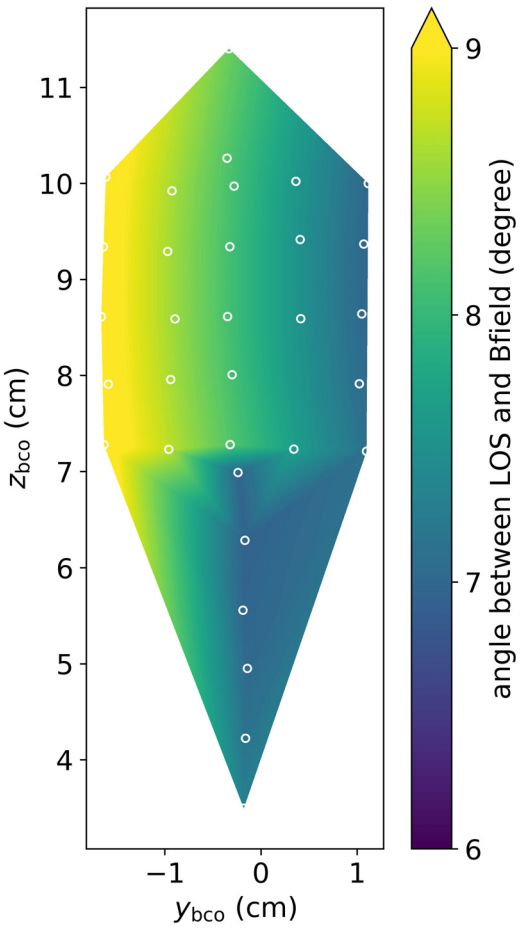


FIG. 18. The angle between the lines of sight and the magnetic field line, displayed in the z_{bco}–y_{bco} plane. It is calculated for #40425 and t = 4.78 s.

3. Connection length for the given equilibrium

In Fig. 20, the connection length taken from the midplane is calculated.

4. Comparison of background profiles with and without filaments

In Fig. 21, two background profiles for temperature and density each are plotted. The profiles without any exclusion of filaments take all time points of the interval into account. In contrast to this, the other profiles are calculated discarding the time points with intensities above 2.5σ. For these profiles, the time point is discarded if it is on any radial position above the threshold. In addition, the two time points before and after are discarded as well. As a result,

04 November 2026 08:21:20

© Author(s) 2023

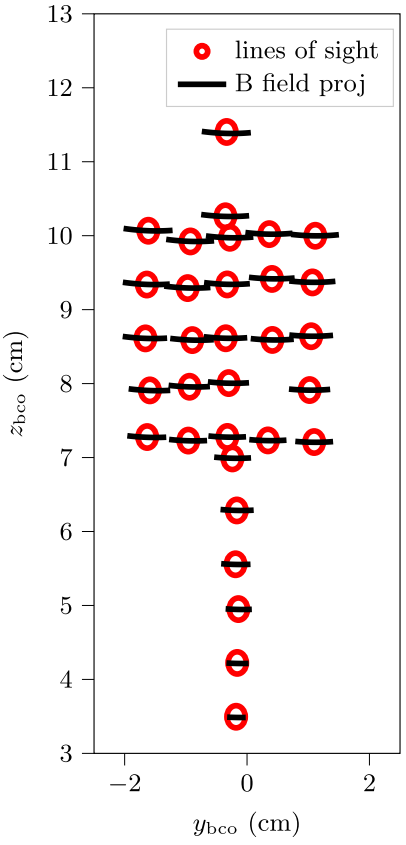


FIG. 19. The figure shows the positions of the lines of sight (diameter of 3 mm) in red. The black lines are the projection of the magnetic field (from #40425, $t = 4.78$ s) in the z_{bco}–y_{bco} plane. The total magnetic field is still approximately parallel to x_{bco}. It shows that a single magnetic field lines does not hit multiple LOS.

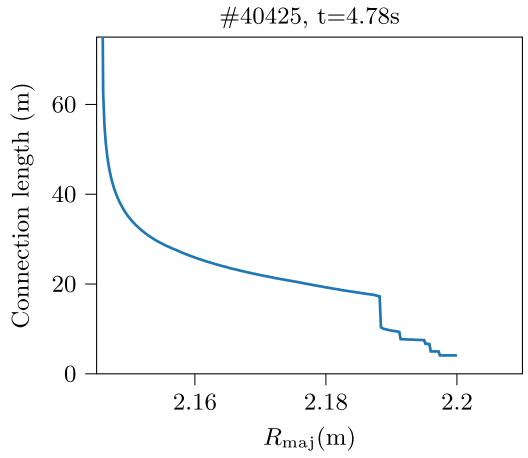


FIG. 20. The connection length (inner to outer divertor) over the midplane radius for the given magnetic equilibrium. The step at $R_{maj} = 2.195$ m is caused by the field lines hitting a limiter. At $R_{maj} = 2.145$ m, the field lines diverge through the secondary/upper X-point.

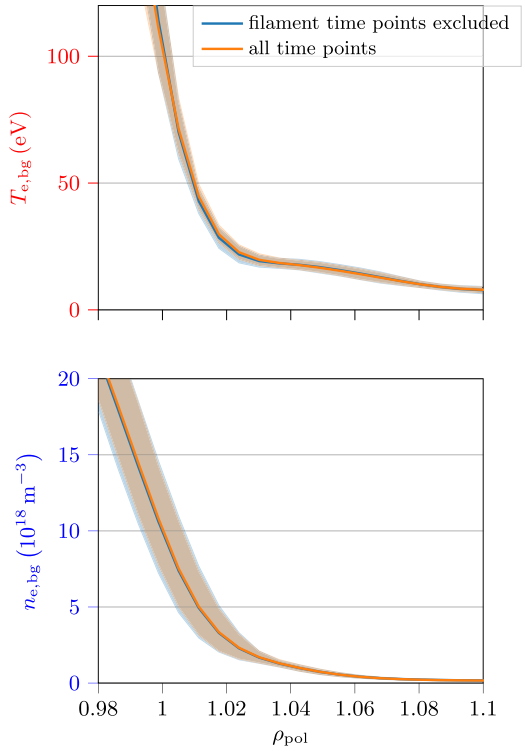


FIG. 21. Comparison between the background profiles, once calculated with and once without filament time points. They are taken from #40425, $t = 4.78$ s – 5.78 s.

12% of the time points are discarded. It can be seen that discarding filament time points makes for the selected discharge no difference for the time averaged profiles.

5. Line ratios and intensities for the reconstructed filament

For the evaluated timepoint discussed in Sec. V, the curves for the reconstructed data compared to the experimental measurement are displayed in Figs. 22–25. In each plot, the black line corresponds to the measured values, also showing its standard deviation. The five plots are sorted according to the poloidal position of the LOS. "HEBxx + 4" corresponds to the 5 lines of sight with the highest y_{bco} value. The next ones are the "HEBxx + 02" LOS, continuing the steps till "HEBxx-4." For "HEBxx + 0," additional radial LOS are displayed, which are not used in the reconstruction.

The exp. data (black line) are the measurement for the selected conditionally averaged filament. The background case (blue line) corresponds to the case, where solely the background is used to calculate the intensities and line ratios with the forward model, i.e., it is assumed that no filament is present there. For the reconstructed case (red line), the reconstructed filament amplitude is added on top of the background, showing the final result of the reconstruction. In practical, all cases, the reconstructed intensities and line ratios match the experimental data better than the background case.

04 November 2026 08:21:20

© Author(s) 2023

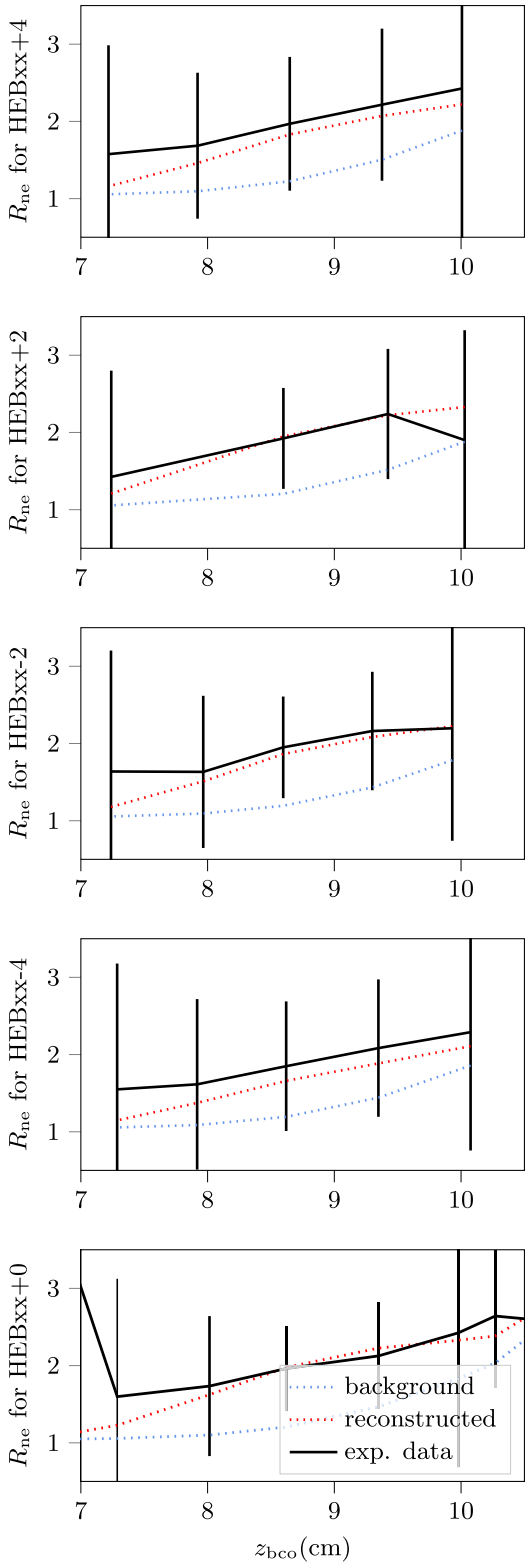


FIG. 22. Result of the reconstruction for $\Delta t = 0\ \mu$s, displayed for $R_{ne} = \frac{I_{667}}{I_{728}}$.

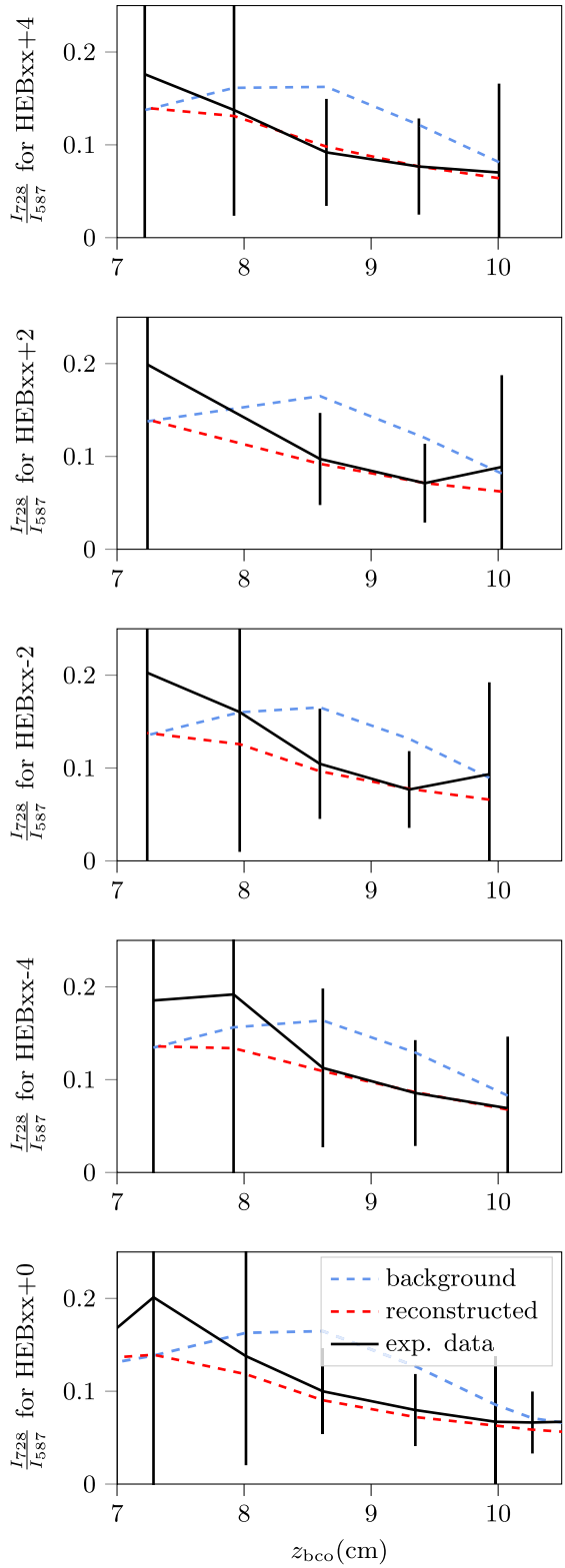


FIG. 23. Result of the reconstruction for $\Delta t = 0\ \mu$s, displayed for $\frac{I_{728}}{I_{587}}$.

04 November 2026 08:21:20

© Author(s) 2023

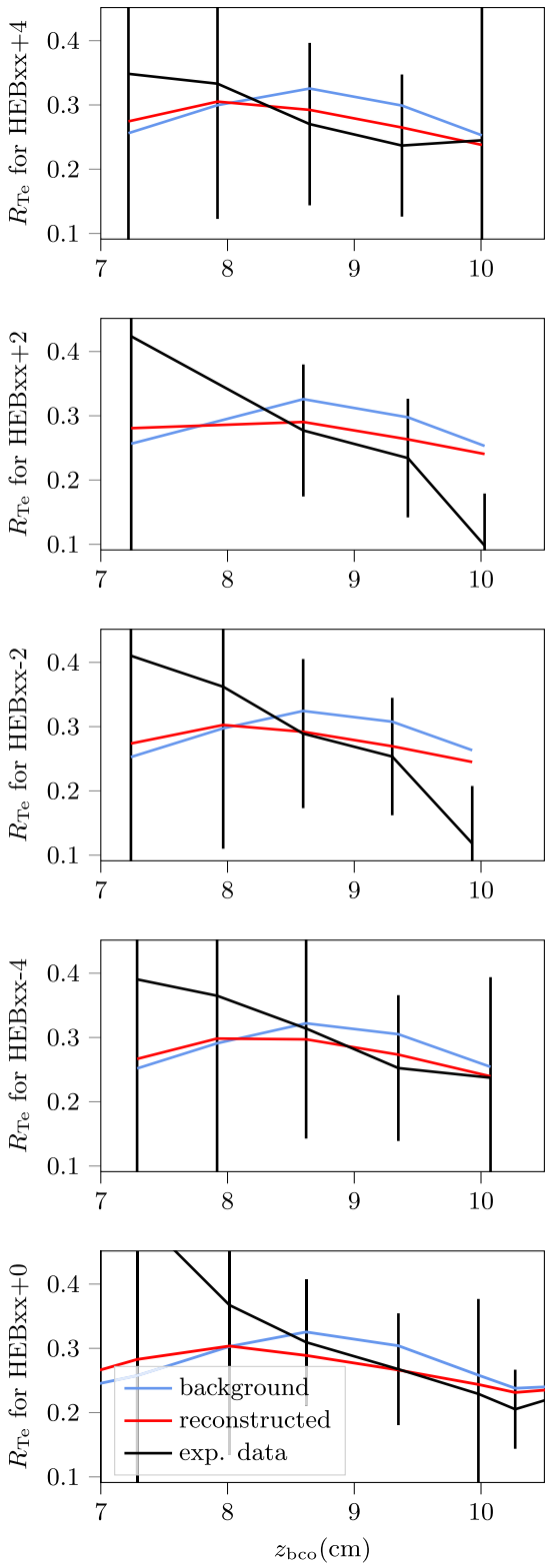


FIG. 24. Result of the reconstruction for $\Delta t = 0$ μs, displayed for $R_{Te} = \frac{I_{728}}{I_{706}}$.

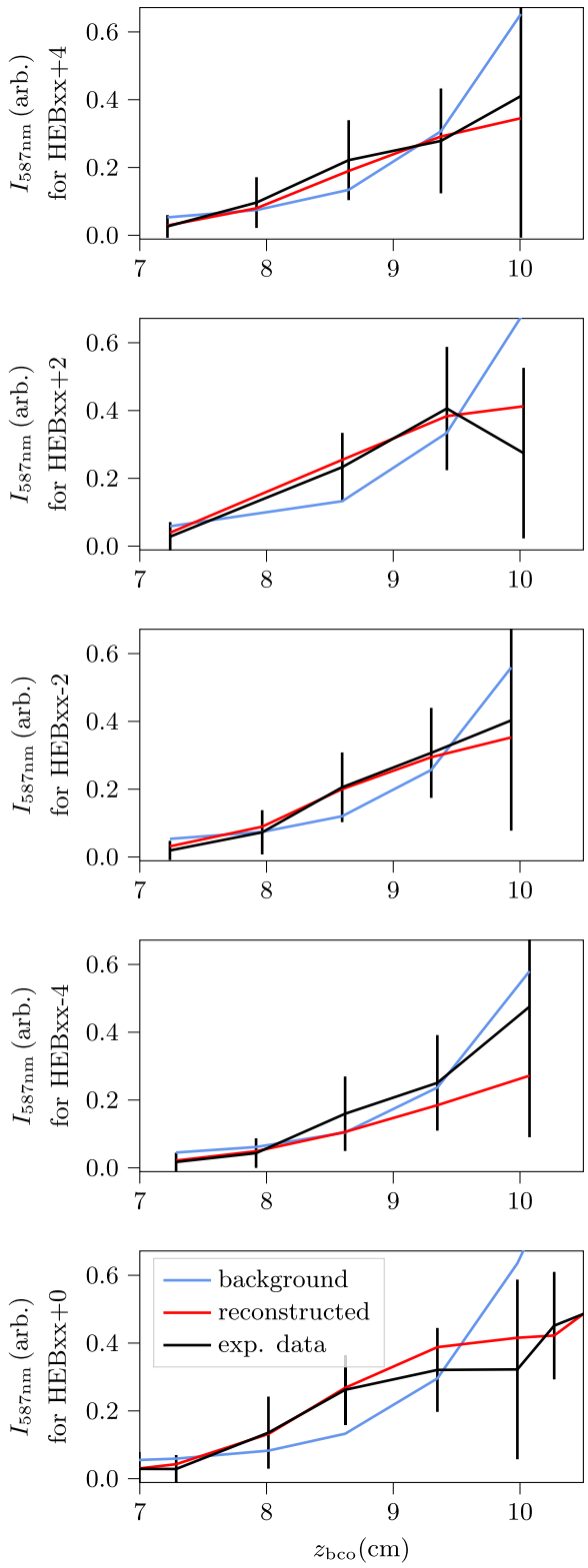


FIG. 25. Result of the reconstruction for $\Delta t = 0$ μs, displayed for I_{587}.

04 November 2026 08:21:20

© Author(s) 2023

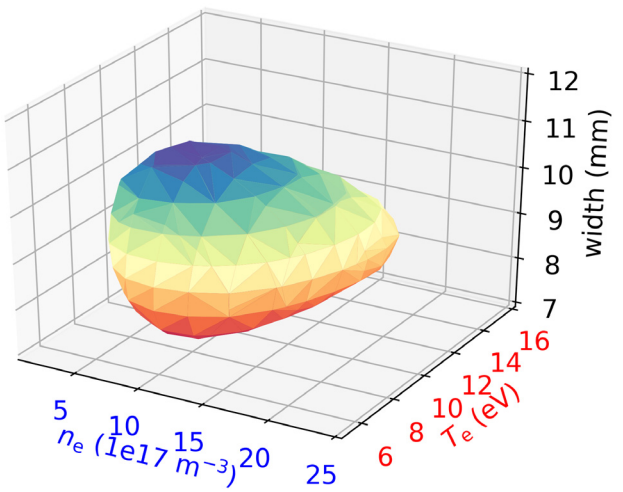


FIG. 26. The figure shows the surface of the cost function, representing one standard deviation. The color is another indicator for the width, used to pronounce the 3D shape. It can be seen that the values are correlated, since the body lies obliquely in the temperature-density plane and both parameters are strongly correlated with the width of the filament.

6. Correlation between the reconstructed parameters

The parameters of the filament are strongly correlated, which is indicated in Fig. 26. There, the case for $\Delta t = 0\,\mu s$ is displayed.

7. Temperature and density decay model

For the density, the assumed decay is purely caused by convection,

$$\frac{dn_e}{dt} = \frac{-\Gamma \cdot A}{A \cdot L_c} = \frac{-n_e \cdot c_s}{L_c}, \tag{A1}$$

calculated from the ion sound speed $c_s = \sqrt{\frac{T_e + \gamma T_i}{m_i}}$ with an adiabatic coefficient of $\gamma = 3$. In addition to the ion sound speed, the decay only depends on the parallel connection length L_c.

The temperature decay is calculated from the temporal derivative of the filament energy,

$$W_{fil} = A \cdot L_c \cdot n_e \cdot T_e.$$

By calculating the temporal derivatives of the filament energy W_{fil} and assuming transport without sources and sinks ($\frac{dn_e}{dt} = 0$), the temperature decay results are

$$\frac{dT_e}{dt} = \frac{\frac{dW_{fil}}{dt}}{A \cdot L_c \cdot n_e} = \frac{-Q}{A \cdot L_c \cdot n_e} = \frac{-q_\parallel}{L_c \cdot n_e}. \tag{A2}$$

The parallel heat flow in the conduction case[55] is given as

$$q_{\parallel,\mathrm{cond.}} = \frac{2}{7}\frac{1}{L_c}\hat{\kappa}_e T_e^{\frac{7}{2}}, \tag{A3}$$

with the assumption $T_{target} = 0\,\mathrm{eV}$ and the upstream temperature T_e.

In the sheath connected case, the parallel heat flow is given as

$$q_{\parallel,\mathrm{conv.}} = \gamma_{t,e} \cdot T_e \cdot 0.5 \cdot \Gamma, \tag{A4}$$

with the electron energy transmission coefficient $\gamma_{t,e} = 5.35$.[56]

REFERENCES

[1] D. A. D'Ippolito, J. R. Myra, and S. J. Zweben, Phys. Plasmas **18**, 060501 (2011).
[2] M. Griener, E. Wolfrum, G. Birkenmeier, M. Faitsch, R. Fischer, G. Fuchert, L. Gil, G. Harrer, P. Manz, D. Wendler, and U. Stroth, Nucl. Mater. Energy **25**, 100854 (2020).
[3] N. Ben Ayed, A. Kirk, B. Dudson, S. Tallents, R. G. L. Vann, and H. R. Wilson, Plasma Phys. Controlled Fusion **51**, 035016 (2009).
[4] M. Spolaore, K. Kovařík, J. Stöckel, J. Adamek, R. Dejarnac, I. Duran, M. Komm, T. Markovic, E. Martines, R. Panek, J. Seidl, and N. Vianello, Nucl. Mater. Energy **12**, 844–851 (2017).
[5] S. I. Krasheninnikov, Phys. Lett. A **283**, 368–370 (2001).
[6] J. R. Myra, D. A. Russell, and D. A. D'Ippolito, Phys. Plasmas **13**, 112502 (2006).
[7] P. Manz, D. Carralero, G. Birkenmeier, H. W. Müller, S. H. Müller, G. Fuchert, B. D. Scott, and U. Stroth, Phys. Plasmas **20**, 102307 (2013).
[8] J. A. Boedo, J. Nucl. Mater. **390–391**, 29–37 (2009).
[9] S. I. Krasheninnikov, D. A. D'Ippolito, and J. R. Myra, J. Plasma Phys. **74**, 679–717 (2008).
[10] G. Fuchert, G. Birkenmeier, D. Carralero, T. Lunt, P. Manz, H. W. Müller, B. Nold, M. Ramisch, V. Rohde, and U. Stroth, Plasma Phys. Controlled Fusion **56**, 125001 (2014).
[11] C. Wüthrich, C. Theiler, N. Offeddu, D. Galassi, D. Oliveira, B. Duval, O. Février, T. Golfinopoulos, W. Han, E. Marmar, J. L. Terry, C. Tsui, and TCV Team. Nucl. Fusion **62**, 106022 (2022), preprint 2203.10907.
[12] S. J. Zweben, J. L. Terry, D. P. Stotler, and R. J. Maqueda, Rev. Sci. Instrum. **88**, 041101 (2017).
[13] J. Yuan, B. Yuan, M. Xu, Y. Yu, L. Nie, R. Ke, Z. Wang, S. Gong, T. Wu, Y. Wu, T. Long, H. Wang, H. Liu, and W. Yue, Plasma Sci. Technol. **21**, 084002 (2019).
[14] E. de la Cal, Nucl. Fusion **56**, 106031 (2016).
[15] C. Killer, B. Shanahan, O. Grulke, M. Endler, K. Hammond, and L. Rudischhauser, Plasma Phys. Controlled Fusion **62**, 085003 (2020).
[16] N. Vianello, D. Carralero, C. Tsui, V. Naulin, M. Agostini, I. Cziegler, B. Labit, C. Theiler, E. Wolfrum, D. Aguiam, S. Allan, M. Bernert, J. A. Boedo, S. Costea, H. De Oliveira, O. Fevrier, J. Galdon-Quiroga, G. Grenfell, A. Hakola, C. Ionita, H. Isliker, A. Karpushov, J. Kovacic, B. Lipschultz, R. Maurizio, K. McClements, F. Militello, A. Nielsen, J. Olsen, J. Rasmussen, T. Ravensbergen, H. Reimerdes, B. Schneider, R. Schrittwieser, E. Seliunin, M. Spolaore, K. Verhaegh, J. Vicente, N. Walkden, and W. Zhang, Nucl. Fusion **60**, 016001 (2020).
[17] N. Offeddu, W. Han, C. Theiler, T. Golfinopoulos, J. L. Terry, E. Marmar, C. Wüthrich, C. Tsui, H. de Oliveira, B. Duval, D. Galassi, D. Oliveira, D. Mancini, and TCV Team. Nucl. Fusion **62**, 096014 (2022).
[18] G. Birkenmeier, F. M. Laggner, M. Willensdorfer, T. Kobayashi, P. Manz, E. Wolfrum, D. Carralero, R. Fischer, B. Sieglin, G. Fuchert, and U. Stroth, Plasma Phys. Controlled Fusion **56**, 075019 (2014).
[19] S. Zoletnik, G. Anda, C. Biedermann, D. Carralero, G. Cseh, D. Dunai, C. Killer, G. Kocsis, A. Krämer-Flecken, M. Otte, B. Shanahan, T. Szepesi, M. Vecsei, and L. Zsuga, Plasma Phys. Controlled Fusion **62**, 014017 (2020).
[20] J. A. Boedo, D. L. Rudakov, R. A. Moyer, S. I. Krasheninnikov, D. G. Whyte, G. R. McKee, G. Tynan, M. J. Schaffer, P. C. Stangeby, P. West, S. Allen, T. Evans, R. Fonck, E. Hollmann, A. Leonard, A. Mahdavi, G. Porter, M. Tillack, and G. Antar, Phys. Plasmas **8**, 4826–4833 (2001).
[21] D. L. Rudakov, J. A. Boedo, R. A. Moyer, S. I. Krasheninnikov, A. W. Leonard, M. A. Mahdavi, G. R. McKee, G. D. Porter, P. C. Stangeby, J. G. Watkins, W. P. West, D. G. Whyte, and G. Antar, Plasma Phys. Controlled Fusion **44**, 308 (2002).
[22] B. LaBombard, Phys. Plasmas **9**, 1300–1311 (2002).

04 November 2026 08:21:20

© Author(s) 2023

[23]E. Calderón, C. Hidalgo, M. A. Pedrosa, and C. Silva, Rev. Sci. Instrum. **75**, 4293–4295 (2004).
[24]O. Schmitz, I. L. Beigman, L. A. Vainshtein, B. Schweer, M. Kantor, A. Pospieszczyk, Y. Xu, M. Krychowiak, M. Lehnen, U. Samm, and B. Unterberg, Plasma Phys. Controlled Fusion **50**, 115004 (2008).
[25]J. M. Muñoz-Burgos, M. Agostini, P. Scarin, D. P. Stotler, E. A. Unterberg, S. D. Loch, O. Schmitz, K. Tritz, and D. Stutman, Phys. Plasmas **23**, 053302 (2016).
[26]M. Agostini, P. Scarin, R. Cavazzana, L. Carraro, L. Grando, C. Taliercio, L. Franchin, and A. Tiso, Rev. Sci. Instrum. **86**, 123513 (2015).
[27]D. Wendler, R. Dux, R. Fischer, M. Griener, E. Wolfrum, G. Birkenmeier, U. Stroth, and Team t A U, Plasma Phys. Controlled Fusion **64**, 045004 (2022).
[28]M. Griener, E. Wolfrum, M. Cavedon, R. Dux, V. Rohde, M. Sochor, J. M. Muñoz-Burgos, O. Schmitz, and U. Stroth, Rev. Sci. Instrum. **89**, 10D102 (2018).
[29]M. Griener, J. M. Muñoz-Burgos, M. Cavedon, G. Birkenmeier, R. Dux, B. Kurzan, O. Schmitz, B. Sieglin, U. Stroth, E. Viezzer, and E. Wolfrum, Plasma Phys. Controlled Fusion **60**, 025008 (2018).
[30]M. Griener, O. Schmitz, K. Bald, D. Bösser, M. Cavedon, P. De Marné, T. Eich, G. Fuchert, A. Herrmann, A. Kappatou, T. Lunt, V. Rohde, B. Schweer, M. Sochor, U. Stroth, A. Terra, and E. Wolfrum, Rev. Sci. Instrum. **88**, 033509 (2017).
[31]K. Sawada, Y. Yamada, T. Miyachika, N. Ezumi, A. Iwamae, and M. Goto, Plasma Fusion Res. **5**, 1 (2010).
[32]D. Carralero, M. Siccinio, M. Komm, S. Artene, F. D'Isa, J. Adamek, L. Aho-Mantila, G. Birkenmeier, M. Brix, G. Fuchert, M. Groth, T. Lunt, P. Manz, J. Madsen, S. Marsen, H. Müller, U. Stroth, H. Sun, N. Vianello, M. Wischmeier, and E. Wolfrum, Nucl. Fusion **57**, 056044 (2017).
[33]A. S. Thrysøe, A. S. Poulsen, and M. Wiesenberger, Phys. Plasmas **30**, 012302 (2023).
[34]M. Willensdorfer, G. Birkenmeier, R. Fischer, F. M. Laggner, E. Wolfrum, G. Veres, F. Aumayr, D. Carralero, L. Guimarãis, and B. Kurzan, Plasma Phys. Controlled Fusion **56**, 025008 (2014).
[35]D. P. Stotler, S. Ku, S. J. Zweben, C. Chang, R. Churchill, and J. L. Terry, Nucl. Mater. Energy **19**, 113–119 (2019).
[36]D. P. Stotler, S. Ku, S. J. Zweben, C. S. Chang, R. M. Churchill, and J. L. Terry, Phys. Plasmas **27**, 062512 (2020).
[37]M. Griener, J. Kalis, D. Wendler, G. Birkenmeier, E. Wolfrum, R. M. McDermott, and U. Stroth, Nucl. Mater. Energy **34**, 101346 (2023).
[38]E. Brochu, V. M. Cora, and N. de Freitas, "A tutorial on Bayesian optimization of expensive cost functions, with application to active user modeling and hierarchical reinforcement learning," arXiv:1012.2599 (2010).
[39]G. D. Conway, C. Angioni, F. Ryter, P. Sauter, and J. Vicente, Phys. Rev. Lett. **106**, 065001 (2011).
[40]D. Réfy, E. R. Solano, N. Vianello, S. Zoletnik, D. Dunai, B. Tál, M. Brix, R. Gomes, G. Birkenmeier, E. Wolfrum, F. M. Laggner, M. Griener, O. Asztalos, and E. Delabie, Nucl. Fusion **60**, 056004 (2020).
[41]E. R. Solano, N. Vianello, E. Delabie, J. Hillesheim, P. Buratti, D. Réfy, I. Balboa, A. Boboc, R. Coelho, B. Sieglin, S. S. Silburn, P. Drewelow, S. Devaux, D. Dodt, A. Figueiredo, L. Frassinetti, S. Marsen, L. Meneses, C. F. Maggi, J. Morris, S. Gerasimov, M. Baruzzo, M. Stamp, D. Grist, I. Nunes, F. Rimini, S. Schmuck, I. Lupelli, and C. Silva, Nucl. Fusion **57**, 022021 (2017).
[42]O. Grulke, J. L. Terry, B. LaBombard, and S. J. Zweben, Phys. Plasmas **13**, 012306 (2006).
[43]Y. H. Xu, S. Jachmich, R. R. Weynants, and Team t T, Plasma Phys. Controlled Fusion **47**, 1841–1855 (2005).
[44]G. Xu, V. Naulin, W. Fundamenski, C. Hidalgo, J. Alonso, C. Silva, B. Gonçalves, A. Nielsen, J. Juul Rasmussen, S. I. Krasheninnikov, B. Wan, and M. Stamp, Nucl. Fusion **49**, 092002 (2009).
[45]G. S. Kirnev, V. P. Budaev, S. A. Grashin, E. V. Gerasimov, and L. N. Khimchenko, Plasma Phys. Controlled Fusion **46**, 621–637 (2004).
[46]H. Johnsen, H. L. Pecseli, and J. Trulsen, Phys. Fluids **30**, 2239 (1987).
[47]H. Johnsen, H. L. Pecseli, and J. Trulsen, Plasma Phys. Controlled Fusion **28**, 1519 (1986).
[48]M. Kočan, F. P. Gennrich, A. Kendl, and H. W. Müller, Plasma Phys. Controlled Fusion **54**, 085009 (2012).
[49]M. Kočan, J. P. Gunn, M. Komm, J. Y. Pascal, E. Gauthier, and G. Bonhomme, Rev. Sci. Instrum. **79**, 073502 (2008).
[50]L. Spitzer and R. Härm, Phys. Rev. **89**, 977–981 (1953).
[51]D. A. D'Ippolito, J. R. Myra, and S. I. Krasheninnikov, Phys. Plasmas **9**, 222–233 (2002).
[52]G. Birkenmeier, P. Manz, D. Carralero, F. M. Laggner, G. Fuchert, K. Krieger, H. Maier, F. Reimold, K. Schmid, R. Dux, T. Pütterich, M. Willensdorfer, and E. Wolfrum, Nucl. Fusion **55**, 033018 (2015).
[53]W. Fundamenski and R. A. Pitts, Plasma Phys. Controlled Fusion **48**, 109–156 (2006).
[54]D. Moulton, P. Ghendrih, W. Fundamenski, G. Manfredi, and D. Tskhakaya, Plasma Phys. Controlled Fusion **55**, 085003 (2013).
[55]P. Stangeby, *The Plasma Boundary of Magnetic Fusion Devices*, Plasma Phys ed. (CRC Press, Bristol; Philadelphia, PA, 2000).
[56]U. Stroth, *Plasmaphysik*, 2nd ed. (Springer Berlin Heidelberg, Berlin, Heidelberg, 2018).
[57]D. Stroth *et al.*, Nucl. Fusion **62**, 042006 (2022).

04 November 2026 08:21:20

© Author(s) 2023